Noise generation of graded poroelastic edges from vortex rings

by

Huansheng Chen

A Dissertation

Presented to the Graduate and Research Committee

of Lehigh University

in Candidacy for the Degree of

Doctor of Philosophy

in

Mechanical Engineering

Lehigh University

January 2024

Date	
Dave	
Accepted Date	
accepted Date	
	Dr. Justin W. Jaworski, Advisor
	Committee Mem
	Dr. Arindam Banerjee
	Dr. Donald O. Rockwell
	Dr. Keith W. Moored
	Dr. Yue Yu

To my family

Acknowledgements

I am indebted to many people who over these past several years have informed my view on research, aeroacoustics, fluid mechanics, mathematics, machine learning, career and much more. Perhaps most of all, I am grateful that they have made my growth in these areas a journey that I will look back on so fondly.

I must first and foremost express my sincere gratitude to my advisor, Dr. Justin W. Jaworski, for his tireless support at every stage of my PhD. His mathematical and physical insight has been incredibly valuable, and he has always been able to provide timely assistance when I was stuck in research. He has always made time to answer my questions and walked me through complex math derivations. In additional to these, I also remember the moments he spent teaching me about writing and presenting, giving career advice, or cracking a witty joke. I feel privileged to have been supervised by such a brilliant, elegant and considerate professor. Justin, thank you for bringing me such a fruitful and memorable PhD journey.

I must also thank Dr. Yue Yu for bringing me into the world of peridynamics and machine learning, where I got a chance to work with Drs. Nathaniel Trask and Marta D'Elia at the Sandia National Laboratories. She is a brilliant applied mathematician with great patience during all of the math and programming problems I have encountered with my research.

I am also grateful for the excellent support from my dissertation committee: Professors Arindam Banerjee, Donald Rockwell, Keith Moored, and Yue Yu. Their thoughtful criticism and exacting standards have enriched greatly my dissertation research and the

enjoyment and value of my graduate education.

I must also acknowledge the various sources of funding that have supported this work. My PhD was generously supported by the National Science Foundation under awards 1804445 and 1805692, and was also supported by J. David A. Walker and M. Elizabeth Walker Endowed Fellowship, Rossin College Doctoral Fellowship Award, and various teaching assistantships offered by the Department of Mechanical Engineering and Mechanics at Lehigh University. I must also thank the Office of International Affairs at Lehigh University for providing the Doctoral Travel Grant for Global Opportunities (DTG-GO) for travel to international conferences.

Last but not the least, I must thank my parents for their endless supports that make my PhD journey be possible. I also want to thank my wife Vanessa who has always been with me during this PhD journey.

Declaration

This dissertation describes research carried out in the Department of Mechanical Engineering & Mechanics of Lehigh University. The analysis in Chapter 3 and results in Chapter 4 have been presented at AIAA conference proceeding as Chen & Jaworski [10] and at APS DFD meetings [9, 58], and have recently been published as Chen et al. [11]. Also, part of Chapter 1 may be found in the Introduction of Chen et al. [11]. The figures in §4.1.4 are reproduced with permission from Yoas [60].

Huansheng Chen

November 2023

Nomenclature

angle of the rectilinear path of vortex ring α open area fraction α_H open area fraction at the leading edge α_L open area fraction at the trailing edge α_T vorticity, $(\omega_1, \omega_2, \omega_3)$ ω observer location, (x_1, x_2, x_3) \boldsymbol{x} projection of y on the (y_1, y_2) -plane \boldsymbol{Y} source location, (y_1, y_2, y_3) \boldsymbol{y} δ Dirac delta function intrinsic fluid loading parameter, $\rho_f k/mk_B^2$ ϵ Γ strength of vortex ring \mathcal{G} gamma function nondimensional porosity parameter, $\alpha_H \overline{K}_R/kR$ μ/k angular frequency ω \overline{K}_R nondimensional Rayleigh conductivity, $2K_R/(\pi R)$

- \bar{t} nondimensional time, Ut/L
- Φ stream function
- Π acoustic power
- Ψ velocity potential
- ψ angle of incident plane wave
- ρ' density perturbation
- ρ density, $\rho_0 + \rho'$
- ρ_0 mean density
- ρ_f fluid density
- curl curl operator
- div divergence operator
- σ vortex core radius
- θ angle of observation
- \widehat{G}_e frequency-domain Green's function for a semi-infinite impermeable elastic edge
- \widehat{G}_0 frequency-domain Green's function for incident field
- \widehat{G}_{rp} frequency-domain Green's function for a semi-infinite uniformly porous rigid edge
- \widehat{G}_s frequency-domain Green's function for scattered field
- a vortex ring radius
- c_0 speed of sound
- g(t) temporal function of acoustic pressure for non-elastic edges
- G_e time-domain Green's function for a semi-infinite impermeable elastic edge

 G_0 time-domain Green's function for incident field

 G_{rp} time-domain Green's function for a semi-infinite uniformly porous rigid edge

 G_s time-domain Green's function for scattered field

I acoustic intensity

k wavenumber, ω/c_0

 k_B in vacuo bending wavenumber

 K_R Rayleigh conductivity

L nearest distance between the vortex ring path and the edge

m(t) temporal function of acoustic pressure for elastic edges

M Mach number

p' pressure perturbation

P total far-field noise, dB

p pressure, $p_0 + p'$

 p_0 mean pressure

R radius of circular pore aperture

t time

 t_r retarded time, $t - x/c_0$

 T_{ij} Lighthill stress tensor

U vortex ring speed

 v_{ξ} complex velocity in the ξ direction

Y magnitude of Y

Contents

A	ckno	wledgements	v
D	eclar	ation	vii
N	onme	enclature	viii
Li	st of	Tables	xiv
Li	st of	Figures	xv
\mathbf{A}	bstra	ıct	1
1	Intr	roduction	3
	1.1	Background	3
	1.2	Major unresolved issues and technical approach	5
	1.3	Statement of purpose	7
	1.4	Dissertation outline	7
2	Ma	thematical foundations	9
	2.1	Wave equation	9
	2.2	Helmholtz equation	10
	2.3	Acoustic compactness	11
	2.4	Acoustic sources	11
	2.5	Free-space Green's function	12

		2.5.1	Time-domain representation	12
		2.5.2	Frequency-domain representation	13
	2.6	Recip	rocal theorem	14
	2.7	Acous	tic power and intensity	15
	2.8	Vortex	sound at low Mach numbers	15
		2.8.1	Lighthill's equation	15
		2.8.2	Powell-Howe acoustic analogy	16
3	Aco	oustic s	scattering from poroelastic edges	19
	3.1	Semi-i	nfinite edge with uniform properties	19
		3.1.1	Model problem	20
		3.1.2	Porous edge	21
		3.1.3	Elastic edge	29
	3.2	Semi-i	nfinite edge with non-uniform properties	31
		3.2.1	Model problem	32
		3.2.2	Mathieu function collocation method	33
		3.2.3	Kinematic boundary condition	35
4	Res	${ m ults}$		36
	4.1	Unifor	emly-porous rigid edge	36
		4.1.1	Impermeable limit	36
		4.1.2	High-porosity limit	37
		4.1.3	General porosity case	39
		4.1.4	Comparison with experimental measurements from ARL	41
	4.2	Imper	meable elastic edge	48
		4.2.1	Asymptotic limit $k\epsilon^{-1/2} \ll 1$	49
	4.3	Semi-i	nfinite edge with non-uniform properties	50
		4.3.1	Numerical verification for uniformly-porous rigid edge	52
		4.3.2	Graded porous rigid edge	53

5	Conclusions	56
A	Green's function for a uniformly-porous edge	58
В	Green's function for an uniformly-elastic edge	62
\mathbf{C}	First derivative of the temporal function of acoustic pressure, $\dot{g}(s)$	63
D	Estimate of vortex-edge interaction time	64
${f E}$	Analyticity of the proposed stream function	66
\mathbf{F}	Derivations of derivatives of vortex ring speed: $\mathbf{D}_{\overline{t}}v_{\xi}(C)$ and $\mathbf{D}_{\overline{t}}^{2}v_{\xi}(C)$	68
Bi	ography	79

List of Tables

4.1	Radiated acoustic power scaling as a function of offset distance L with se-	
	lected varying observation angle θ	46
4.2	Dimensionless porosity parameter values μ/k used in the numerical verifica-	
	tion of Mathieu function collocation method	52
4.3	Dimensionless porosity parameter value μ/k used in the graded porosity con-	
	figuration	53

List of Figures

3.1	Schematic of the poroelastic half-plane and vortex ring source	21
3.2	Sideview of the poroelastic half-plane and schematic of a vortex ring source	26
3.3	Schematic of the finite, graded porous plate and source	33
4.1	Time history of acoustic pressure waveform for the impermeable rigid edge	
	case	38
4.2	Time history of acoustic pressure waveform for the highly-porous edge case	40
4.3	Acoustic directivity and corresponding source waveforms with different porosity	41
4.4	Dependence of a coustic power scaling exponents γ and v on dimensionless	
	porosity parameter μ/k	42
4.5	Schematic of two plate configurations in the vortex-ring experiments	43
4.6	Theoretical-experimental comparisons of the acoustic power scaling on the	
	vortex ring speed U	44
4.7	Experimental result of acoustic directivity for vortex ring sound from an	
	impermeable rigid edge	45
4.8	Experimental result of acoustic directivity for vortex ring sound from a	
	highly-porous edge case	46
4.9	Experimental results of temporal acoustic pressure waveforms for the imper-	
	meable rigid edge $(\mu/k=0)$	48
4.10	Experimental results of temporal acoustic pressure waveforms for the highly-	
	porous edge $(\mu/k = 58.9)$	49

4.11	Time history of acoustic pressure waveform for the elastic edge case $\ \ \dots \ \ \dots$	51
4.12	Theoretical-numerical comparisons of acoustic directivity with different poros-	
	ity μ/k	52
4.13	Numerical comparison of acoustic directivity for uniform and linearly-graded	
	porosity cases	54
4.14	Numerical comparison of acoustic directivity for different frequencies	55
A.1	Dependence of wavenumber parameter m on the dimensionless porosity pa-	
	rameter μ/k	61
D.1	Schematic for the estimation of vortex-edge interaction time in experiments	65

Abstract

The sound generated by an acoustic source near a semi-infinite edge with uniform parameters is studied theoretically. The acoustic emission of a vortex ring passing near a semi-infinite porous or elastic edge with uniform properties is formulated as a vortex sound problem and is solved using a Green's function approach. The time-dependent pressure signal and its directivity in the acoustic far field are determined analytically for rigid porous edges as a function of a single dimensionless porosity parameter. At large values of this dimensionless parameter, the radiated acoustic power scales on the vortex ring speed Uand the nearest distance between the edge and the vortex ring L as U^6L^{-5} , in contrast to the U^5L^{-4} scaling recovered in the impermeable edge limit for small porosity values. These analytical findings agree well with the results of a companion experimental campaign conducted at the Applied Research Laboratories (ARL) at Penn State University. A related theoretical analysis of the sound scattered by uniform, impermeable elastic edges admits analytical results in a specific asymptotic limit, in which the acoustic power scales on U^7L^{-6} . In complement to the analysis of vortex ring sound from edges, the acoustic scattering of a turbulent eddy near a finite edge with a graded porosity distribution is determined numerically and is validated against analytical acoustic directivity predictions from the vortex-edge model problem for a semi-infinite edge in the appropriate high frequency limit. The cardioid and dipolar acoustic directivity obtained in the vortex ring configuration for low and high dimensionless porosity parameter values, respectively, are recovered by the numerical approach. An imposed linear porosity distribution demonstrates no substantial difference in the acoustic directivity relative to the uniformly porous cases at high

porosity parameter values, where the local porosity parameter value at the edge determines the scattered acoustic field. However, more modulated behavior of the acoustic directivity is found at a relatively low frequency for the case of a finite edge with small graded porosity distribution.

Chapter 1

Introduction

1.1 Background

The pioneering aeroacoustics analysis by Lighthill [46] first determined that isolated turbulent eddies in low-speed flows produce sound in a quadrupolar directivity pattern with an intensity that is proportional to U^3M^5 or U^8 , where U and M are the characteristic flow speed and Mach number, respectively. The close proximity of turbulence to a solid body amplifies its acoustic intensity and changes the directivity pattern of the scattered sound: Curle [21] showed that the radiated acoustic power of turbulence scattered by acoustically-compact bodies scales on U^6 , which is a factor of M^{-2} increase in magnitude for low Mach number flows that is accompanied by a shift to dipolar directivity. Flowes Williams & Hall [25] examined analytically a more efficient noise generation scenario of turbulent eddies near a non-compact sharp edge, where the acoustic power scales on U^5 , i.e., M^{-3} louder than free-field turbulence; a cardioid directivity pattern for pressure accompanies this change in acoustic intensity, which scales on the distance L between the turbulent eddy and the edge as L^{-3} . A sharp edge may be generalized geometrically into a wedge, where Crighton & Leppington [20] showed that a finite opening angle weakens the acoustic field relative to the U^5 velocity scaling for classical trailing-edge noise.

The efficient conversion of turbulence energy into sound by rigid-impermeable edges

continues to motivate strategies to disrupt the noise-generation process through the modification of trailing edge material properties. Crighton & Leppington [19] carried out one of the first such analytical investigations by imposing a point-reacting impedance condition on a semi-infinite plate, where in certain parametric limits the plate may be considered as either rigid or limp. The rigid limit recovers the results of Ffowcs Williams & Hall [25], and the so-called 'limp' edge limit produces a U^6 power scaling and dipolar acoustic field that would be expected for turbulence noise produced by a compact body or a solid body without an edge. More sophisticated models including flexural waves in a compliant edge that were not considered by Crighton & Leppington [19] have since been investigated to study their effect on structural [15] and aerodynamic noise [6, 7, 32, 33, 34, 35], including the influence of structural resonance on radiated sound for finite elastic sections [1, 2, 45].

Porosity is a common design approach to mitigate noise generation that manipulates the edge boundary condition. Ffowcs Williams [24] determined that turbulence noise from an infinite perforated screen scales on U^6 and has a dipolar directivity in a high-porosity limit, which Nelson [52] corroborated experimentally for a porous surface away from its edges. Howe [30] later examined the sound generation of a vortex passing near a semi-infinite plate with a finite porous extension and showed that the porous section reduces the sound level by relaxing the abrupt change in boundary conditions at the impermeable edge. Kisil & Ayton [43] constructed an analysis procedure for this configuration and underscored the importance of secondary scattering from the impermeable-porous junction for high-frequency turbulence sources. In addition to these analytical works, the effect of porosity on edge noise reduction has been investigated computationally [42] and experimentally [26, 27], and has been reviewed recently by Jaworski & Peake [40].

Further research attention has been directed toward the combination of porosity and elasticity reduces turbulence edge noise. Jaworski & Peake [39] analysed the scaling behavior of turbulence sound radiated by semi-infinite poroelastic edges using the Wiener-Hopf analysis technique. They recovered the U^6 acoustic power scaling and the dipole directivity results of Ffowcs Williams [24] in the high-porosity limit for an infinite perforated

sheet, indicating that the effect of the edge on the acoustic scaling behavior is eliminated in this case. In other words, the acoustical non-compactness of an impermeable edge is disrupted by surface porosity, which permits near-field fluid motions through the edge that are associated with an acoustic dipole.

Jaworski & Peake [39] also identified a new U^7 velocity scaling for elastic edges under specific fluid loading conditions. With the aim to relax the semi-infinite geometrical restriction, Cavalieri et al. [8] developed a boundary element method to determine numerically how sound scatters from a finite poroelastic strip or flat-plate airoil. Porosity reduced noise more effectively at low frequencies with wavelengths that are large relative to the airfoil chord length, while elasticity was more effective at high-frequency noise reduction. Therefore, poroelasticity may enable broadband noise reduction for finite edge sections or airfoils. More recent investigations and extensions involving finite geometries include a finite one-dimensional rigid plate with a poroelastic extension [3], multiple finite plates with various material properties [12, 13], and generalized two-dimensional poroelastic plates with straight, swept, or serrated edges [54].

1.2 Major unresolved issues and technical approach

It is well-established [17] that the presence of a rigid and impermeable edge near a turbulent region of fluid results in a significant increase in the noise generated by that turbulence in low-Mach-number flows. Analytical and numerical results outlined in the previous section suggest that this noise generation process may be mitigated by the modification of edge material properties to make the edge porous, elastic, or poroelastic. The U^5 acoustic power and cardioid directivity predictions by Ffowcs William & Hall [25] for a rigid and impermeable edge has been confirmed by the empirical study of Brooks & Hodgson [5] and several other measurement campaigns [see 17]. However, direct experimental confirmation of the U^6 and U^7 scalings for highly porous or elastic edges, respectively, is not likely possible in conventional aeroacoustic facilities due to secondary flow noise contributions that may become as loud or louder than the edge noise itself. For example, turbulent boundary

layers present on wind tunnel walls and test article surfaces produce roughness noise [22] with a dipolar directivity and an intensity that also scales on U^6 [31]. Therefore, the mean flow associated with the turbulent boundary layer that generates edge noise is also a source of acoustic contamination relative to sound produced at porous or elastic edges: in a scaling sense, edge noise in the high-porosity limit would be indistinguishable from roughness noise, which would dominate all together the weaker U^7 sound from elastic edges in the appropriate parametric limit.

To circumvent this critical limitation, an alternative approach is proposed using a moving vortex ring as an acoustic source in an otherwise quiescent fluid. The replacement of the turbulence source with a coherent vortex structure is motivated by the seminal analysis of Crighton [16], which determined analytically that a line vortex moving round an edge that produces the same U^5 intensity scaling determined by wave scattering analyses [25, 19], where U is the vortex ring speed in this configuration. The matched asymptotic results by Crighton [16] were further examined and verified by Howe [29] using a low-frequency Green's function and by Möhring [49] using a vector Green's function. Kambe et al. [41] validated the vortex sound approach by achieving the U^5 intensity scaling using a vortex ring shot rectlinearly past a rigid, impermeable edge and confirmed its cardioid directivity. Their analysis of vortex ring sound obtained an L^{-4} intensity scaling based on the minimum distance between the vortex path and the edge, which is distinct from the scaling of Ffowcs Williams & Hall [25] for turbulence scattering and is particular to the vortex ring configuration. Crucially, the vortex ring configuration of Kambe et al. [41] does not require a background mean flow and therefore does not introduce flow noise sources that would potentially corrupt an acoustic measurement of the edge noise emission.

In addition to this critical unresolved issue, it is worth noting that the numerical work by Cavalieri et al. [8] identified a large performance difference in noise reduction between low and high Helmholtz numbers, i.e., the product of the acoustic wavenumber (frequency) and chord length. Therefore, it begs the question as for whether non-uniform distribution of edge properties (such as graded porosity or elasticity) could possess a different and tunable

performance in noise reduction compared to the uniform edge case. Due to the fundamental technical challenge that the traditional analytical approach cannot handle non-uniform edge conditions, the corresponding acoustic problem for non-uniform edge properties is solved numerically using the Mathieu function collocation approach of Colbrook & Priddin [14] for finite panels, which allows arbitrary edge conditions and also permits a numerical verification of findings from the uniform edge-noise analysis.

1.3 Statement of purpose

This dissertation pursues theoretical models of a vortex ring passing near a semi-infinite porous or elastic edge to enable experimental validation of acoustic power scaling results by analogy and confirmation of directivity shapes predicted by previous acoustic scattering works for poroelastic edges. Analytical predictions are achieved in closed form or in particular parametric asymptotic limits to guide companion acoustic experiments at the Applied Research Laboratory (ARL) at Penn State University, where the vortex ring analysis in the time domain enables additional results of comparisons of the acoustic signal to constitute a full validation. In addition to the associated experimental comparisons, this work also seeks verification of the analytical results based on a novel numerical method proposed by Colbrook & Priddin [14]. Furthermore, this dissertation explores how these acoustic scattering results are modified by a spatial gradient in the porosity distribution near the edge to motivate further experimental campaigns.

1.4 Dissertation outline

In pursuit of these goals, the present work seeks to address the following research questions.

• What are the findings (acoustic scaling, acoustic directivity, acoustic pressure waveforms, etc) on the vortex-edge acoustic model problem with uniform edge distribution?

- Does vortex-edge acoustic model recover the results of previous turbulence-edge acoustic models?
- What is the difference between the analytical model and the numerical model?
- What are the limitations of the numerical model in pursuit of the verification of analytical results?
- What are the new findings of the numerical model?
- How does the modification of edge property affect the results for a trailing edge acoustic model problem?

The remainder of this dissertation is outlined as follows: Chapter 2 introduces briefly the related acoustic theory and mathematical foundations used in this work. Chapter 3 outlines the vortex sound model and constructs the associated Green's function to estimate the acoustic emission of a vortex ring passing near a porous or elastic edge with uniform properties, as well as discuss the numerical approach pursued for non-uniform properties. Chapter 4 discusses results from the mathematical models in Chapter 3 in the context of their parametric limits for different edge conditions, their influence on the directivity and acoustic intensity scaling behaviors, and comparisons with associated experimental measurements. Conclusions and final remarks are presented in Chapter 5.

Chapter 2

Mathematical foundations

2.1 Wave equation

Sound is longitudinal fluctuations in pressure that propagate through a medium, where these fluctuations may be created by vibrating bodies, turbulent flows, or other unsteady phenomena. It is often the case in acoustic applications that the pressure fluctuations associated with the acoustic waves are small relative to the mean undisturbed pressure. Therefore, the equations of motion may be linearized and described by the linear wave equation for sound propagation, where the sound is assumed to propagate through a stationary fluid of uniform mean density ρ_0 and pressure p_0 . The wave equation for a stationary fluid may also be used to describe the acoustics in a low-speed flow, where convective effects at small Mach number would be a higher-order effect [37].

Let the linear perturbations of density and pressure from their mean values be denoted by ρ' and p', where $\rho'/\rho_0 \ll 1$, $p'/p_0 \ll 1$. Linearizations of the inviscid momentum equation and continuity equation yield [37, pp. 5 - 6]

$$\left(\frac{1}{c_0^2}\frac{\partial^2}{\partial t^2} - \nabla^2\right)p' = \rho_0 \frac{\partial q}{\partial t} - \operatorname{div} \mathbf{F},\tag{2.1}$$

which describe the production of sound by a volume source q and a body force \mathbf{F} , which is herein neglected.

The unsteady motion can be described by a velocity potential ϕ , which satisfies

$$\mathbf{v} = \nabla \phi, \quad p' = \rho' c_0^2 = -\rho_0 \frac{\partial \phi}{\partial t}.$$
 (2.2)

Substitution (2.2) into (2.1) yields the linear wave equation,

$$\left(\frac{1}{c_0^2}\frac{\partial^2}{\partial t^2} - \nabla^2\right)\phi = -q(\boldsymbol{x}, t). \tag{2.3}$$

Note that sound waves propagating outside the source region (where $q(\boldsymbol{x},t)=0$) are governed by the homogeneous form of (2.3).

2.2 Helmholtz equation

The linearity of the wave equation allows acoustic solutions to be superposed for acoustic sources with different frequency components, which permits the full solution to be expressed as a Fourier series or integral.

Consider the sound propagated into an unbounded, stationary fluid from a time-harmonic volume source $q(\mathbf{x},t) = q(\mathbf{x},\omega)e^{-i\omega t}$ of angular frequency ω . The velocity potential governed by (2.3) should oscillate at the same frequency, that is $\phi(\mathbf{x},t) = \phi(\mathbf{x},\omega)e^{-i\omega t}$. The linear wave equation in (2.3) may now be transformed into its frequency form, which is the inhomogeneous Helmholtz equation:

$$(k^2 + \nabla^2) \phi = q(\mathbf{x}, \omega), \tag{2.4}$$

where $k = \omega/c_0$ is the acoustic wavenumber, and the solution of velocity potential must exhibit outgoing wave behavior.

2.3 Acoustic compactness

The acoustic energy produced by the sound source will behave differently depending on the distance between the observer and an acoustic source. Therefore the acoustic field may be separated into two regions, near field and far field. The acoustic compactness of the source region itself is set by a dimensionless combination kl of the acoustic wavenumber of radiated sound $k = \omega/c_0$ and the characteristic length of the source l. In the acoustic near field where $kl \ll 1$, the source dimension is smaller than the wavelength of the sound it emits, therefore the acoustic source is considered *compact* and point-like, which can be treated as a simple monopole source. In the acoustic far field where $kl \gg 1$, the acoustic source vibrates at a high frequency, which is considered a non-compact source. Similarly, a scattering body is considered *compact* when its characteristic length is smaller than the wavelengths of the sound it produces or with which it interacts.

2.4 Acoustic sources

Compact acoustic sources, whose acoustic wavelength is much greater than its feature size (see §2.3), may be represented as a monopole, dipole or quadrupole, or higher-order multipole, or as a combination of these sources. For example, a monopole source represents a radially pulsating sphere in the limit of a vanishing radius, and the source strength is uniform in all directions. The source distribution of a point monopole in the linear wave equation in (2.3) is given by

$$q(\mathbf{x},t) = Q(t)\delta(\mathbf{x}),\tag{2.5}$$

where the source strength is denoted by Q(t), and $\delta(x)$ represents the pulsating behavior. For a unit-strength monopole, Q(t) = 1.

A point dipole is formed by two monopole sources of equal strength that are out of phase and separated by a distance of less than an acoustic wavelength. In contrast to a single monopole, there is no net introduction of fluid by a dipole, therefore a dipole is a weaker radiator of sound than a monopole. It is the net force on the fluid which causes energy to be radiated in the form of sound waves. The source distribution of a point dipole in the linear wave equation in (2.3) can be represented by

$$q(\boldsymbol{x},t) = \operatorname{div}\left[\boldsymbol{f}(t)\delta(\boldsymbol{x})\right] = \frac{\partial}{\partial x_j}\left[f_i(t)\delta(\boldsymbol{x})\right], \tag{2.6}$$

where f(t) is a time-dependent vector, and the index j runs over Cartesian coordinates x_i , x_j .

A quadrupole source consists of two identical dipoles, with opposite phase and separated by small distance. In the case of the quadrupole, there is no net flux of fluid and no net force on the fluid, the fluctuating stress on the fluid that generates the sound waves. However, since fluids do not support shear stresses well, quadrupoles are poor radiators of sound. The source distribution of a point quadrupole in the linear wave equation in (2.3) is generally in the form

$$q(\boldsymbol{x},t) = \frac{\partial^2 T_{ij}}{\partial x_i \partial x_j}(\boldsymbol{x},t), \tag{2.7}$$

where T_{ij} is the second-order stress tensor, and the indices i, j run over Cartesian coordinates x_i, x_j .

2.5 Free-space Green's function

2.5.1 Time-domain representation

The free-space Green's function $G(x, y, t - \tau)$ is the particular solution of the linear wave equation (2.3) generated by an impulsive unit point source $\delta(x - y)\delta(t - \tau)$, located at source point x = y at time $t = \tau$. Accordingly, the free-space Green's function in time domain is determined by

$$\left(\frac{1}{c_0^2}\frac{\partial^2}{\partial t^2} - \boldsymbol{\nabla}^2\right)G(\boldsymbol{x}, \boldsymbol{y}, t - \tau) = \delta(\boldsymbol{x} - \boldsymbol{y})\delta(t - \tau), \tag{2.8}$$

where $G(\boldsymbol{x}, \boldsymbol{y}, t - \tau) = 0$ for $t < \tau$.

The acoustic solution of the linear wave equation for an impulsive point source at x and at time t is [37]

$$\phi(\boldsymbol{x},t) = \frac{1}{4\pi|\boldsymbol{x}|} \delta\left(t - \frac{|\boldsymbol{x}|}{c_0}\right),\tag{2.9}$$

which indicates that the sound wave vanishes everywhere for t < 0 and exhibits outgoing wave behavior.

Therefore, the solution for free-space Green's function $G(\boldsymbol{x}, \boldsymbol{y}, t - \tau)$ in (2.8) is obtained from (2.9) by replacing \boldsymbol{x} by $\boldsymbol{x} - \boldsymbol{y}$ and t by $t - \tau$,

$$G(\boldsymbol{x}, \boldsymbol{y}, t - \tau) = \frac{1}{4\pi |\boldsymbol{x} - \boldsymbol{y}|} \delta\left(t - \tau - \frac{|\boldsymbol{x} - \boldsymbol{y}|}{c_0}\right), \tag{2.10}$$

which represents an impulsive, spherically-symmetric wave prapagating away from the source at y at the speed of sound c_0 , and the wave amplitude decreases with increasing observer-source distance |x - y|.

2.5.2 Frequency-domain representation

The free-space Green's function $\widehat{G}(\boldsymbol{x},\boldsymbol{y},\omega)$ in frequency domain is the solution for the Helmholtz equation (2.4) for a unit point source $q(\boldsymbol{x},\omega)=\delta(\boldsymbol{x}-\boldsymbol{y}),$

$$(k^2 + \nabla^2) \widehat{G}(\boldsymbol{x}, \boldsymbol{y}, \omega) = \delta(\boldsymbol{x} - \boldsymbol{y}). \tag{2.11}$$

Recalling the governing equation of the free-space Green's function in the time domain in (2.8), and applying the Fourier integral formula

$$\delta(t - \tau) = \frac{1}{2\pi} \int_{-\infty}^{\infty} e^{-i\omega(t - \tau)} d\omega, \qquad (2.12)$$

(2.8) becomes

$$(k^{2} + \nabla^{2}) \left\{ \int_{-\infty}^{\infty} G(\boldsymbol{x}, \boldsymbol{y}, t - \tau) e^{i\omega t} dt \right\} = -e^{i\omega \tau} \delta(\boldsymbol{x} - \boldsymbol{y}).$$
 (2.13)

It is then straightforward to determine

$$\widehat{G}(\boldsymbol{x}, \boldsymbol{y}, \omega) = -\int_{-\infty}^{\infty} G(\boldsymbol{x}, \boldsymbol{y}, t - \tau) e^{i\omega(t - \tau)} dt,$$
(2.14)

and the substitution of (2.10) into the integrand of (2.14) yields

$$\widehat{G}(\boldsymbol{x}, \boldsymbol{y}, \omega) = -\frac{1}{4\pi |\boldsymbol{x} - \boldsymbol{y}|} e^{ik|\boldsymbol{x} - \boldsymbol{y}|}.$$
(2.15)

2.6 Reciprocal theorem

Solutions of the Helmholtz equation for point sources satisfy a reciprocal theorem, which is a special case of a very general theorem of mechanics that was stated in the context of acoustics by Lord Rayleigh [57].

Consider the two acoustic problems where sound is generated by two unit point sources at $\mathbf{x} = \mathbf{x}_A$ and $\mathbf{x} = \mathbf{x}_B$ in the presence of a solid body S. Let the velocity potentials of the resulting acoustic fields be denoted as $\widehat{G}(\mathbf{x}, \mathbf{x}_A, \omega)$ and $\widehat{G}(\mathbf{x}, \mathbf{x}_B, \omega)$, respectively, where

$$(k^2 + \nabla^2) \widehat{G}(\mathbf{x}, \mathbf{x}_A, \omega) = \delta(\mathbf{x} - \mathbf{x}_A), \tag{2.16}$$

$$(k^2 + \nabla^2) \widehat{G}(\boldsymbol{x}, \boldsymbol{x}_B, \omega) = \delta(\boldsymbol{x} - \boldsymbol{x}_B). \tag{2.17}$$

The reciprocal theorem states that

$$\widehat{G}(\boldsymbol{x}_A, \boldsymbol{x}_B, \omega) = \widehat{G}(\boldsymbol{x}_B, \boldsymbol{x}_A, \omega). \tag{2.18}$$

That is, the acoustic solution observed at x_A produced by the point source at x_B is equal to the solution at x_B produced by an equal point source at x_A . This statement has a

simple proof, which may be found in Rayleigh [57, pp. 145-148] or in other reference texts on acoustics [23, 37, 51].

2.7 Acoustic power and intensity

The acoustic power Π is the total acoustic energy radiated by a source or source distribution, which is determined by the formula

$$\Pi = \oint_{S} p v_r dS = \oint_{S} \frac{p^2}{\rho_0 c_0} dS, \qquad (2.19)$$

where the integration is over the surface S of a large sphere of radius r centered on the source region. The integral may be calculated easily if the pressure and velocity are known to order 1/r on S, as the surface area is $4\pi r^2$. Therefore, the formula $v_r = p/\rho_0 c_0$ always holds at large distances r from the center of the sphere (source region), where the wavefronts may be locally regarded as planar.

The acoustic intensity I is defined as the acoustical energy carried by sound waves per unit of area of the wavefront. For spherical waves on the surface of the large sphere of radius r, the corresponding acoustic intensity I is

$$I = pv_r = \frac{p^2}{\rho_0 c_0}. (2.20)$$

2.8 Vortex sound at low Mach numbers

2.8.1 Lighthill's equation

The sound generated by flow-borne disturbance such as turbulence is termed aerodynamic sound. The modern theory of aerodynamic sound was pioneered by Lighthill [46], where in his study of sound generation by a turbulent nozzle flow, Lighthill transformed the Navier-Stokes and continuity equations into an *exact* (i.e., no assumption is made),

inhomogeneous wave equation [46],

$$\left(\frac{1}{c_0^2}\frac{\partial^2}{\partial t^2} - \nabla^2\right)c_0^2\rho' = \frac{\partial^2 T_{ij}}{\partial x_i \partial x_j},$$
(2.21)

where ρ' is the fluid density fluctuation ($\rho' = \rho - \rho_0$), and c is the isentropic speed of sound. T_{ij} is the so-called Lighthill stress tensor described by

$$T_{ij} = \rho v_i v_j + \left[(p - p_0) - c_0^2 (\rho - \rho_0) \right] \delta_{ij} - \sigma_{ij}, \tag{2.22}$$

which indicates that the sound generated by free turbulence is exactly equivalent to that produced in the ideal, stationary fluid forced by a distribution of quadrupole sources.

2.8.2 Powell-Howe acoustic analogy

In the present work where the flow region is limited to low Mach numbers $(M \ll 1)$ and large Reynolds numbers, i.e.

$$p - p_0 - c_0^2(\rho - \rho_0) \approx (p - p_0)(1 - c_0^2/c^2) \approx O(M^2),$$
 (2.23)

and viscous dissipation may be neglected. Therefore, T_{ij} may be approximated by the Reynolds stress term $\rho v_i v_j$.

By taking $c = c_0$ and $\rho = \rho_0$, the Lighthill's equation may now be rearranged as

$$\left(\frac{1}{c_0^2}\frac{\partial^2}{\partial t^2} - \nabla^2\right)c_0^2\rho' = \rho_0 \frac{\partial^2 v_i v_j}{\partial x_i \partial x_j}.$$
(2.24)

However, it is still challenging to use (2.24) directly due to the nonlinear Reynolds stress term on the right hand side of the corresponding equation.

For the present vortex-sound problem at low Mach numbers, the Biot-Savart induction formula relates the vorticity and velocity fields:

$$v(x,t) = \operatorname{curl} \int \frac{\omega(y,t)d^3y}{4\pi|x-y|},$$
 (2.25)

where the integration over the entire spatial domain is implied.

The value of Lighthill's quadrupole source distribution in (2.24) can be approximated as

$$\rho_0 \frac{\partial^2 v_i v_j}{\partial x_i \partial x_j} = \rho_0 \operatorname{div} (\boldsymbol{\omega} \times \boldsymbol{v}), \tag{2.26}$$

which is the principal source of sound at low Mach numbers. Substitution of (2.26) into (2.24) yields

$$\left(\frac{1}{c_0^2}\frac{\partial^2}{\partial t^2} - \nabla^2\right)c_0^2 \rho' = \rho_0 \operatorname{div}(\boldsymbol{\omega} \times \boldsymbol{v}).$$
(2.27)

Howe [29] reformulated (2.27) by taking the total enthalpy,

$$B = \int \frac{\mathrm{d}p}{\rho} + \frac{1}{2}v^2, \tag{2.28}$$

as an independent acoustic variable to replace the pressure fluctuation term $c_0^2 \rho'$ in (2.27) to account for the role of vorticity in the production of sound.

The total enthalpy comes naturally from the Crocco's form of the momentum equation [37]

$$\frac{\partial \mathbf{v}}{\partial t} + \boldsymbol{\omega} \times \mathbf{v} + \nabla B = -\nu \left(\operatorname{curl} \boldsymbol{\omega} - \frac{4}{3} \nabla (\operatorname{div} \mathbf{v}) \right), \tag{2.29}$$

where the vector $(\boldsymbol{\omega} \times \boldsymbol{v})$ is termed the Lamb vector [44].

In irrotational flow Crocco's equation (2.29) reduces to

$$\frac{\partial \mathbf{v}}{\partial t} + \nabla B = 0, \tag{2.30}$$

which implies

$$B = -\frac{\partial \phi}{\partial t}$$
 in regions where $\omega = 0$. (2.31)

 ϕ is the velocity potential that determines the whole motion in the irrotational regions of the fluid. Therefore, B is constant in steady irrotational flow and may be represented by

$$B = \frac{p}{\rho_0} \tag{2.32}$$

if the mean flow is at rest in the acoustic far field.

Taking the time derivative of (2.28) and using Crocco's equation (2.29) with (2.32) leads to

$$\frac{1}{\rho_0} \frac{\partial p}{\partial t} = \frac{DB}{Dt},\tag{2.33}$$

where the viscous correction is ignored at high Reynolds numbers and $\frac{D}{Dt}$ denotes the total derivative.

The governing equation of production of vortex sound at low Mach numbers (without mean flow) is then further proposed by Howe in a simpler form [29],

$$\left(\frac{1}{c_0^2}\frac{\partial^2}{\partial t^2} - \nabla^2\right)B = \operatorname{div}(\boldsymbol{\omega} \times \boldsymbol{v}),\tag{2.34}$$

where in the far field the acoustic pressure p(x,t) is given by the linearized approximation

$$p(\boldsymbol{x},t) = \rho_0 B(\boldsymbol{x},t) = -\rho_0 \iiint (\boldsymbol{\omega} \times \boldsymbol{v})(\boldsymbol{y},\tau) \cdot \frac{\partial G(\boldsymbol{x},\boldsymbol{y},t-\tau)}{\partial \boldsymbol{y}} d^3 \boldsymbol{y} d\tau.$$
 (2.35)

Note that the formula in (2.27) was first proposed by Powell [56] and later elaborated as (2.34) by Howe [29], which is also known as Powell-Howe acoustic analogy. A detailed derivation of this expression may be found in [29].

The significance of the Powell-Howe result (2.35) is that the far-field acoustic pressure can be predicted based on the vorticity distribution in the field and a Green's function for, say, a solid boundary, without the need to know the Reynolds stress as is represented in the Lighthill framework. The Powell-Howe result is used in the next chapter to determine the sound of vortex rings passing near an edge that is porous and/or elastic.

Chapter 3

Acoustic scattering from

poroelastic edges

This chapter studies the sound generation of an acoustic source near a semi-infinite edge with constant or varying parameters by analytical or numerical methods. In §3.1, the sound of a vortex ring passing near a semi-infinite uniformly poroelastic edge is investigated analytically. The vortex sound problem is solved by using Powell-Howe acoustic analogy [36], in which a Green's function approach is introduced to determine the time-dependent acoustic pressure and directivity pattern in the acoustic far field. The Green's functions for different edge properties are solved separately, and scaling laws of vortex ring speed U and the nearest vortex-edge distance L are established using the classical theory of vortex rings. In §3.2, the acoustic scattering of a turbulent eddy near a semi-infinite edge with linearly-graded porosity distribution is considered numerically. The model problem is solved by adapting the Mathieu function collocation method of Colbrook & Priddin [14].

3.1 Semi-infinite edge with uniform properties

The contents of this section are outlined as follows. In §3.1.1, the acoustic problem of a vortex ring interacts with the edge of a semi-infinite poroelastic plate at low Mach numbers

is formulated. In §3.1.2, the Green's function and the vorticity distribution and motion of the vortex ring for a uniformly-porous rigid edge are solved by adapting the previous analyses of Kambe *et al.* [41] and Jaworski & Peake. [39]. In §3.1.3, the Green's function and the vorticity distribution and motion of the vortex ring for an impermeable elastic edge are solved in a similar manner as §3.1.2.

3.1.1 Model problem

Consider a rigid, semi-infinite poroelastic plate with negligible thickness that lies in the region $-\infty < x_1, y_1 \le 0$, $x_2, y_2 = 0$, $-\infty < x_3, y_3 < \infty$ of the coincident Cartesian coordinate systems $\{(x_1, y_1), (x_2, y_2), (x_3, y_3)\}$, as shown in figure 3.1. The poroelastic plate is immersed in an unbounded fluid at rest at infinity. The present research studies the acoustic emission by a vortex ring source passing near the edge of a poroelastic half plane. The Mach number M, defined by U/c_0 , is assumed to be much smaller than unity, where U is the characteristic speed of the vortex ring and c_0 is the sound speed. In present work, acoustic compactness requires $l/\lambda \ll 1$, where l is the characteristic length of the vortex ring and λ is the wavelength of the emitted sound. The source region containing the vortex ring and the edge is therefore considered to be acoustically compact, where the vortex ring is compact, the semi-infinite plate, however is non-compact.

The sound resulting from the vortex ring interaction with a semi-infinite edge may be described by the Powell-Howe acoustic analogy introduced in §2.8, i.e.,

$$\left(\frac{1}{c_0^2} \frac{\partial^2}{\partial t^2} - \nabla^2\right) p = \rho_0 \operatorname{div}(\boldsymbol{\omega} \times \boldsymbol{v}), \tag{3.1}$$

which is a reformulation of Lighthill's theory of aerodynamic sound [46]. Note that the sound source term ρ_0 div $(\boldsymbol{\omega} \times \boldsymbol{v})$ at low Mach number is directly related to the vorticity in the flow field.

Equation (3.1) also admits a general solution in terms of a boundary integral,

$$p(\boldsymbol{x},t) = -\rho_0 \iint (\boldsymbol{\omega} \times \boldsymbol{v})(\boldsymbol{y},\tau) \cdot \frac{\partial G(\boldsymbol{x},\boldsymbol{y};t-\tau)}{\partial \boldsymbol{y}} \,\mathrm{d}\boldsymbol{y} \,\mathrm{d}\tau.$$
 (3.2)

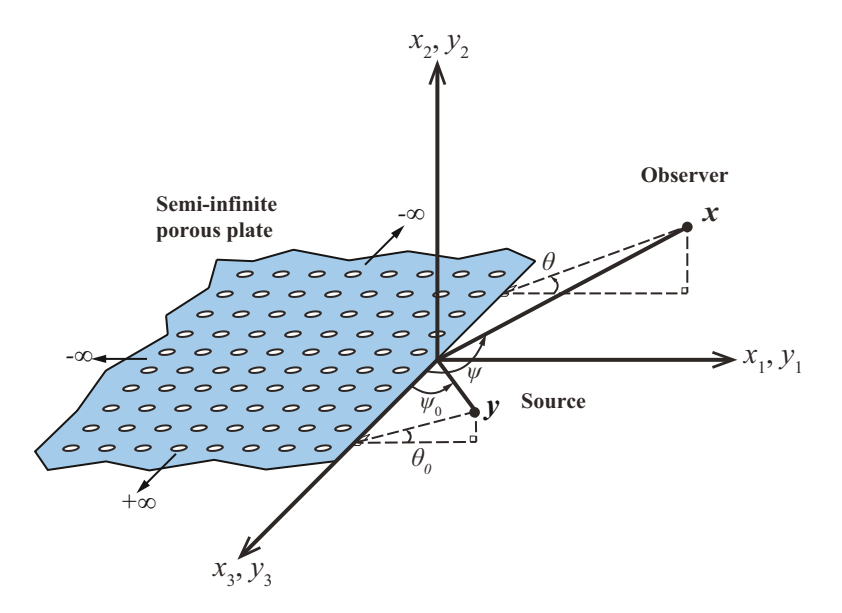


Figure 3.1: Schematic of the poroelastic half-plane and the coincident coordinate systems for the compact vortex ring source $\mathbf{y} = (y_1, y_2, y_3)$ and the observer at $\mathbf{x} = (x_1, x_2, x_3)$.

Here p is the acoustic pressure, ρ_0 is the mean fluid density, ω is the vorticity distribution in an ideal fluid neglecting viscous dissipation, v is the vorticity convection velocity, and $G(x, y; t - \tau)$ is the time-domain Green's function. At sufficiently low Mach numbers, $G(x, y; t - \tau)$ may be approximated by the compact Green's function [29], which is described in the following sections with different edge properties.

3.1.2 Porous edge

In this section, the acoustic emission of a vortex ring passing near a uniformly-porous rigid edge is considered first, which is aim to verify the acoustic scaling and directivity results of Jaworski & Peake [39] with the proposed vortex-ring approach introduced in Chapter 1.

In pursuit of an acoustic pressure prediction using (3.2), two unknown terms must be determined. In §3.1.2.A, the Green's function for a porous rigid edge is solved first. In §3.1.2.B, the vorticity distribution and motion of the vortex ring is then determined using the classical theory of vortex rings.

A Green's function for a porous edge

A Green's function is now sought that produces the solution at distant point $\mathbf{x} = (x_1, x_2, x_3)$ due to an impulsive point source of unit strength at position $\mathbf{y} = (y_1, y_2, y_3)$ near the edge of a porous half plane (see figure 3.1). The Green's function also must exhibit outgoing wave behavior and satisfy [36, p. 39]

$$\left(\frac{1}{c^2}\frac{\partial^2}{\partial t^2} - \boldsymbol{\nabla}^2\right)G_{rp}(\boldsymbol{x}, \boldsymbol{y}; t - \tau) = \delta(\boldsymbol{x} - \boldsymbol{y})\delta(t - \tau), \tag{3.3}$$

where the right-hand side represents the impulsive point source.

The calculation of the compact Green's function in (3.3) may be greatly simplified by application of the reciprocal theorem in (2.18), which implies that the positions of source y and observer x may be interchanged in present model problem (cf. figure 3.1), i.e., the mathematical setup is identical to finding the sound field observed at a near point y due to a monopole at a distant point x. The problem thus converts to the solution for the Green's function G as a function of observer positions y close to the edge, which is a diffraction problem that can be solved in the manner described, for example, by Crighton [19] or Jaworski & Peake [39]. The linearity of (3.3) permits the solution to be written as

$$G_{rp}(\boldsymbol{x}, \boldsymbol{y}; t) = G_{rp}(\boldsymbol{y}, \boldsymbol{x}; t) = G_0(\boldsymbol{y}, \boldsymbol{x}; t) + G_s(\boldsymbol{y}, \boldsymbol{x}; t), \tag{3.4}$$

where $G_0(\boldsymbol{y}, \boldsymbol{x}; t)$ and $G_s(\boldsymbol{y}, \boldsymbol{x}; t)$ are the time-domain velocity potentials for the incident field and the scattered field, respectively. The time-domain Green's function $G_{rp}(\boldsymbol{y}, \boldsymbol{x}; t)$ is related to its Fourier transform $\widehat{G}_{rp}(\boldsymbol{y}, \boldsymbol{x}; k)$ by

$$G_{rp}(\boldsymbol{y}, \boldsymbol{x}; t) = -\frac{1}{2\pi} \int_{-\infty}^{+\infty} \widehat{G}_{rp}(\boldsymbol{y}, \boldsymbol{x}; k) e^{-i\omega t} d\omega.$$
 (3.5)

It is convenient to decompose $\widehat{G}_{rp}(\boldsymbol{y}, \boldsymbol{x}; k)$ into the linear sum $\widehat{G}_{rp}(\boldsymbol{y}, \boldsymbol{x}; k) = \widehat{G}_0(\boldsymbol{y}, \boldsymbol{x}; k) + \widehat{G}_s(\boldsymbol{y}, \boldsymbol{x}; k)$. The expressions for $\widehat{G}_0(\boldsymbol{y}, \boldsymbol{x}; k)$ in (A.3) and $\widehat{G}_s(\boldsymbol{y}, \boldsymbol{x}; k)$ in (A.6) are determined in appendix A using the Wiener-Hopf analysis of Jaworski & Peake [39]. Application of the

Fourier inversion formula (3.5) to these results yields the time-domain Green's functions $G_0(\boldsymbol{y}, \boldsymbol{x}; t)$ and $G_s(\boldsymbol{y}, \boldsymbol{x}; t)$, where $G_0(\boldsymbol{y}, \boldsymbol{x}; t)$ may be expanded in a series form by following the procedure of Kambe *et al.* [41]. The essential results from the reciprocal problem after reverting to the original configuration are:

$$G_0(\boldsymbol{y}, \boldsymbol{x}; t) = \frac{1}{4\pi x} \left(\delta(t_r) + \frac{\boldsymbol{x} \cdot \boldsymbol{y}}{c_0 x} D_t \delta(t_r) + \frac{(\boldsymbol{x} \cdot \boldsymbol{y})^2}{2c_0^2 x^2} D_t^2 \delta(t_r) + \dots \right), \tag{3.6}$$

$$G_s(\boldsymbol{y}, \boldsymbol{x}; t) = \frac{\mu^n}{2\pi^{\frac{3}{2}} c_0^m} \Phi(\boldsymbol{Y}) \frac{M(\psi, \theta)}{x} D_t^m \delta(t_*),$$
(3.7)

where

$$D_t^m \delta(t) = \frac{1}{2\pi} \int_{-\infty}^{+\infty} (-i\omega)^m e^{-i\omega t} d\omega, \quad D_t = \frac{\partial}{\partial t},$$
 (3.8)

$$t_r = t - \frac{x}{c_0}, \quad t_* = t - \frac{1}{c_0} |\mathbf{x} - y_3 \mathbf{k}|,$$
 (3.9)

$$x = |\mathbf{x}|, \quad y = |\mathbf{y}|, \quad \mathbf{k} = (0, 0, 1).$$

Here, $\Phi(\mathbf{Y}) = Y^{\frac{1}{2}} \sin \frac{\theta}{2}$ is the velocity potential about the edge, the projection of \mathbf{y} onto the (y_1, y_2) -plane, and $Y = |\mathbf{Y}|$. The fractional derivative D_t^m is used as a convenient and equivalent means of writing the inverse Fourier transform of the Green's function solution of the scattered sound field. The variables m and n are the exponents of the wavenumber k and the dimensional porosity parameter $\mu = \alpha_H \overline{K}_R/R$. In this parametric group, α_H is the open area fraction of the surface with pores of nominal radius R, and $\overline{K}_R = 2K_R/(\pi R)$, where K_R is the Rayleigh conductivity of the pore [36, 39]; the conditions that the surface is weakly porous and has a pore feature size that is small relative to the acoustic wavelength require $\alpha_H^2 \ll 1$ and $kR \ll 1$, respectively. The directivity function $M(\psi, \theta)$ depends on the angular position of the observer. Note that both $M(\psi, \theta)$ and the exponents m and m vary on the dimensionless porosity parameter μ/k , and must be determined numerically in general. The details are presented in appendix A and are further discussed in §4.

If $G_0(\boldsymbol{y}, \boldsymbol{x}; t)$ in (3.6) is substituted into (3.2), the first two terms of the right-hand side of (3.6) contribute nothing to the sound field due to the vanishing integral around the

half-plane surface, as has been shown previously by Powell [56]. Therefore the total Green's function $G_{rp}(\boldsymbol{y}, \boldsymbol{x}; t) = G_0(\boldsymbol{y}, \boldsymbol{x}; t) + G_s(\boldsymbol{y}, \boldsymbol{x}; t)$ may be approximated to leading order by $G_s(\boldsymbol{y}, \boldsymbol{x}; t)$ only,

$$G_{rp}(\boldsymbol{y}, \boldsymbol{x}; t) \approx \frac{\mu^n}{2\pi^{\frac{3}{2}} c_0^m} \Phi(\boldsymbol{Y}) \frac{M(\psi, \theta)}{x} D_t^m \delta(t_*), \tag{3.10}$$

provided that the third term of $G_0(\boldsymbol{y}, \boldsymbol{x}; t)$ in (3.6) remains subdominant. The form of the Green's function in (3.10) obviates that $\partial G_{rp}(\boldsymbol{y}, \boldsymbol{x}; t)/\partial y_3$ is indeed subdominant to the magnitudes of the derivatives in other two directions, i.e., $\partial G_{rp}(\boldsymbol{y}, \boldsymbol{x}; t)/\partial y_1$ and $\partial G_{rp}(\boldsymbol{y}, \boldsymbol{x}; t)/\partial y_2$. Therefore, the gradient of the Green's function with respect to \boldsymbol{y} , $\partial G_{rp}(\boldsymbol{x}, \boldsymbol{y}; t)/\partial \boldsymbol{y}$, can be approximated by the two-dimensional vector

$$\frac{\partial G_{rp}(\boldsymbol{y}, \boldsymbol{x}; t)}{\partial \boldsymbol{y}} = \frac{\mu^n}{2\pi^{\frac{3}{2}}c^m} \frac{M(\psi, \theta)}{x} D_t \delta(t_*) \left(\frac{\partial}{\partial y_1} \Phi(\boldsymbol{Y}), \frac{\partial}{\partial y_2} \Phi(\boldsymbol{Y}), 0 \right). \tag{3.11}$$

Equation (3.11) may be reworked into a more useful form by introducing the stream function $\Psi(\mathbf{Y})$,

$$\Psi(\mathbf{Y}) = -Y^{\frac{1}{2}}\cos\frac{\theta_0}{2},\tag{3.12}$$

which is related to the velocity potential $\Phi(\mathbf{Y})$ by the Cauchy-Riemann equations,

$$\frac{\partial}{\partial y_1} \Phi(\mathbf{Y}) = \frac{\partial}{\partial y_2} \Psi(\mathbf{Y}), \quad \frac{\partial}{\partial y_2} \Phi(\mathbf{Y}) = -\frac{\partial}{\partial y_1} \Psi(\mathbf{Y}). \tag{3.13}$$

Note that the confirmation of (3.12) to satisfy (3.13) can be found in appendix E, using the velocity potential $\Psi(\mathbf{Y})$ and stream function $\Psi(\mathbf{Y})$ on this edge configuration.

According to Möhring's transformation procedure [49], (3.11) can be rewritten as

$$\frac{\partial G_{rp}(\boldsymbol{y}, \boldsymbol{x}; t)}{\partial \boldsymbol{y}} = \nabla \times (0, 0, G_{rp}(\boldsymbol{y}, \boldsymbol{x}; t))$$

$$= \nabla \times [\Psi(\boldsymbol{Y})\boldsymbol{k}] \frac{\mu^n}{2\pi^{\frac{3}{2}}c_0^m} \frac{M(\psi, \theta)}{x} D_t^m \delta(t_*), \qquad (3.14)$$

where $\mathbf{k} = (0, 0, 1)$. By the substitution of (3.14) into (3.2), the acoustic pressure may be expressed as,

$$p(\boldsymbol{x},t) = -\rho_0 \iint (0, 0, G_{rp}(\boldsymbol{y}, \boldsymbol{x}; t)) \cdot \nabla \times (\boldsymbol{\omega} \times \boldsymbol{v})(\boldsymbol{y}, \tau) \, d\boldsymbol{y} \, d\tau.$$
 (3.15)

The application of incompressible, inviscid vorticity equation [38, p. 158],

$$\frac{\partial \boldsymbol{\omega}}{\partial t} + \nabla \times (\boldsymbol{\omega} \times \boldsymbol{v}) = \mathbf{0},\tag{3.16}$$

and an integration by parts determines the final expression of the acoustic pressure in the far field:

$$p(\boldsymbol{x},t) = \rho_0 D_t \iint \omega_3(\boldsymbol{y},\tau) F(\boldsymbol{x},\boldsymbol{Y}) D_t^m \delta(t_* - \tau) d\boldsymbol{y} d\tau,$$

$$= \rho_0 D_t^{m+1} \int \omega_3(\boldsymbol{y},t_r) F(\boldsymbol{x},\boldsymbol{Y}) d\boldsymbol{y}, \qquad (3.17)$$

where

$$F(\boldsymbol{x}, \boldsymbol{Y}) = \frac{\mu^n}{2\pi^{\frac{3}{2}} c_0^m} \frac{M(\psi, \theta)}{x} \Psi(\boldsymbol{Y}). \tag{3.18}$$

Note that t_* has been replaced by $t_r = t - x/c_0$ in (3.17) for a compact turbulence source. Specific details on the compact vortex ring source and its trajectory are described in the following section.

B Vorticity distribution and vortex ring motion

Consider a thin-cored vortex ring, whose center moves in a plane perpendicular to the y_3 axis, as shown in figure 3.2. O is the coordinate origin located at the half-plane edge, and L is the nearest distance of the vortex ring path to the edge. It is assumed that L is larger than the vortex radius a such that the vortex does not collide with the edge. The unit vector normal to the plane of the vortex ring lies in the (y_1, y_2) -plane, and the ξ axis denotes the vortex path direction. The η axis is taken to be perpendicular to the ξ and y_3

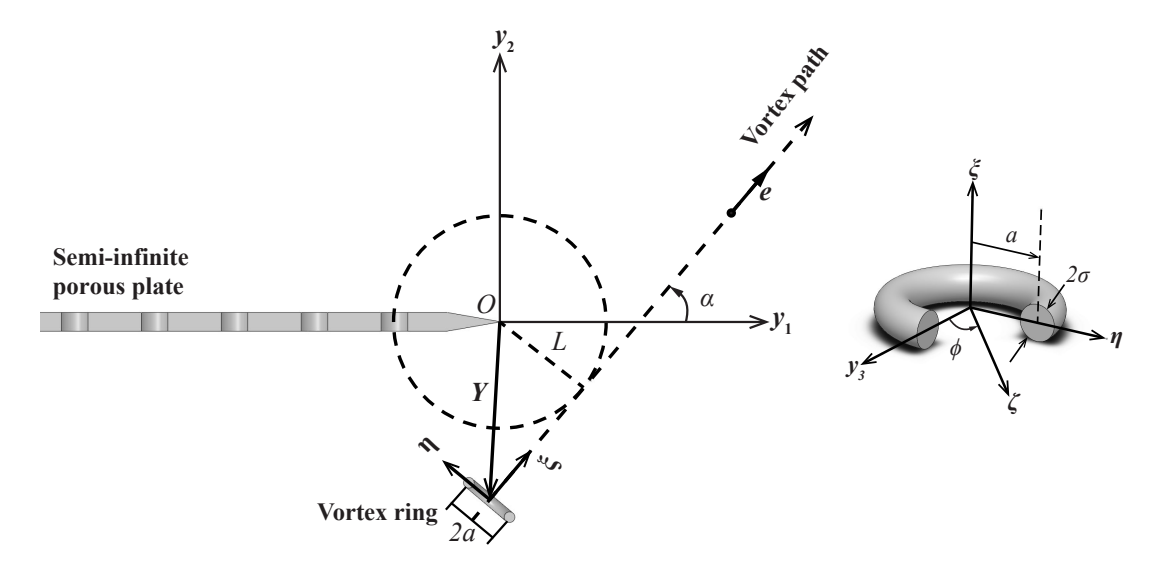


Figure 3.2: Side view of the interaction between a semi-infinite porous plate and a vortex ring convecting on a rectilinear path. The local coordinate system of the vortex ring is illustrated on the right.

axes as illustrated, and the origin of the (ξ, η, y_3) coordinate system is located at the vortex ring centre. The vorticity of the vortex ring is assumed to be concentrated on a circle of radius a with a small vortex core of radius σ , and $\sigma/a \ll 1$. The vorticity components in (ξ, η, y_3) -system are therefore

$$(0, -\Gamma\delta(\xi)\delta(\zeta - a)\sin\phi, \Gamma\delta(\xi)\delta(\zeta - a)\cos\phi), \tag{3.19}$$

where $\zeta = \sqrt{\eta^2 + y_3^2}$, Γ is the fixed strength of the vortex ring, ϕ is the azimuthal angle of the vortex center from the y_3 axis, and ζ is the radial coordinate in the (η, y_3) -plane. This model setup is the same as Kambe *et al.* [41], which in this work permits parametric comparisons against their analysis for an impermeable edge.

Equation (3.17) determines the sound produced by the vortex ring passing near an edge provided that its strength and trajectory are known. Here it is assumed that the vortex ring follows the rectilinear path shown in figure 3.2, which is justified on physical grounds

in appendix C. Direct substitution of (3.19) into (3.17) yields

$$p\left(\boldsymbol{x},t+\frac{x}{c}\right) = \rho_0 \Gamma D_t^{m+1} \int_0^{2\pi} F(\zeta=a,\xi=0;\boldsymbol{C}(t)) a \cos\phi \,d\phi, \tag{3.20}$$

where C(t) represents the position of the vortex centre at time t, and the dependence of F on x has been suppressed here for simplicity. Following the procedure by Kambe et al. [41], F may be approximated by the two-term Taylor expansion with respect to η ,

$$F(\zeta = a, \xi = 0; \mathbf{C}) \approx F(\mathbf{C}) + \frac{\partial}{\partial \eta} F(\mathbf{C}) a \cos \phi.$$
 (3.21)

Using (3.21), the integration in (3.20) produces

$$\int_0^{2\pi} Fa \cos \phi \, d\phi = \pi a^2 \frac{\partial}{\partial \eta} F(\mathbf{C}) = \frac{\pi a^2 \mu^n}{2\pi^{\frac{3}{2}} c_0^m} \frac{M(\psi, \theta)}{x} v_{\xi}(\mathbf{C}), \tag{3.22}$$

where v_{ξ} is the complex velocity of the flow in the ξ direction,

$$v_{\xi} = \frac{\partial}{\partial \eta} \Psi(\mathbf{C}) = \frac{\partial}{\partial \xi} \Phi(\mathbf{C}).$$
 (3.23)

Thus, the acoustic pressure expression is

$$p\left(\boldsymbol{x}, t + \frac{x}{c_0}\right) = \frac{\rho_0 \Gamma \mu^n}{2\pi^{\frac{3}{2}} c_0^m} \frac{M(\psi, \theta)}{x} \mathcal{D}_t^{m+1} [\pi a^2 v_{\xi}(\boldsymbol{C})]. \tag{3.24}$$

Note that $\pi a^2 v_{\xi}$ is the volume flux of the irrotational flow around the edge passing through the vortex ring [37]. It is now clear that the temporal profile of the acoustic pressure signal is proportional to a fractional rate of change of the volume flux through the vortex ring that depends on m. The fractional acceleration of the flow through the vortex ring $D_t^{m+1}[\pi a^2 v_{\xi}(\mathbf{C})]$ must now be evaluated to furnish scaling estimates of the acoustic emission.

Recall that $D_t^{m+1}v_{\xi}(\mathbf{C}) = D_t^m[D_tv_{\xi}(\mathbf{C})]$, and the dimensionless form of $D_tv_{\xi}(\mathbf{C})$ may be

adapted directly from Kambe et al. [41] (see derivation in appendix F),

$$D_{\overline{t}}v_{\xi}(\boldsymbol{C}) = \frac{1}{4}UL^{-\frac{3}{2}}g(\overline{t}), \qquad (3.25)$$

where $\bar{t} = Ut/L$ is the dimensionless time, and

$$g(\bar{t}) = \overline{Y}^{-\frac{3}{2}} \sin\left(\frac{3}{2}\Theta - 2\alpha\right),$$
 (3.26)

$$\overline{Y} = \frac{Y}{L} = (\overline{t}^2 + 1)^{\frac{1}{2}}, \quad \Theta = \tan^{-1} \left(\frac{\overline{t} \sin \alpha \mp \cos \alpha}{\overline{t} \cos \alpha \pm \sin \alpha} \right).$$
 (3.27)

It is clear from (3.25) that $g(\bar{t})$ is proportional to the acceleration of fluid through the vortex ring. Here the time origin $\bar{t} = 0$ denotes the time instant when the vortex ring is at its nearest distance L to the edge.

Therefore, $D_{\bar{t}}^{m+1}v_{\xi}(C)$ in (3.24) may now be expressed as

$$D_{\bar{t}}^{m+1}[v_{\xi}(\mathbf{C})] = \frac{1}{4} U^{m+1} L^{(-m-\frac{3}{2})} D_{\bar{t}}^{m} \left[g\left(\bar{t}\right) \right], \tag{3.28}$$

and the substitution of (3.28), (3.26), and (3.27) into (3.24) yields the acoustic pressure,

$$p\left(\boldsymbol{x},\bar{t}+\frac{x}{c_0}\right) = \frac{\rho_0 \Gamma a^2 \mu^n U^{m+1}}{8\pi^{\frac{1}{2}} c_0^m L^{m+\frac{3}{2}}} \frac{M(\psi,\theta)}{x} \mathcal{D}_{\bar{t}}^m \left[g\left(\bar{t}\right)\right]. \tag{3.29}$$

The undetermined exponents may be shown to be coupled on dimensional grounds, where n is eliminated here using $n + m = \frac{1}{2}$. Also, the velocity U of a vortex ring is proportional to its circulation Γ [44, p. 224]:

$$U = \frac{\Gamma}{4\pi a} \left(\ln \frac{8a}{\sigma} - \frac{1}{4} \right). \tag{3.30}$$

From (3.29), the far-field acoustic pressure radiated by a vortex ring passing near a

porous edge scales on

$$p \sim U^{m+2} L^{-\frac{3}{2}-m},$$
 (3.31)

and the corresponding acoustic power Π is

$$\Pi = \frac{p^2}{\rho_0 c_0} \propto U^{\gamma} L^{-\upsilon},\tag{3.32}$$

where $\gamma = 2m + 4$ and $\upsilon = 2m + 3$.

3.1.3 Elastic edge

The acoustic emission of a vortex ring passing near an impermeable rigid edge is now considered, which aims to validate the acoustic scaling and directivity results of Jaworski & Peake [39] with the proposed vortex-ring approach introduced in Chapter 1.

Similarly, the two unknown terms in (3.2) are determined following the procedures in §3.1.2. In §3.1.3.A, the Green's function for an impermeable elastic edge is determined first. In §3.1.3.B, the vorticity distribution and motion of the vortex ring are then determined using the classical vortex ring theory. It is worth noting that the mathematical derivations in §3.1.3.A and §3.1.3.B are only valid in the asymptotic limit $k\epsilon^{-1/2} \ll 1$, as we only consider the weakest radiated sound for the elastic edge noise problem identified by Jaworski & Peake [39].

A Green's function for an elastic edge $(k\epsilon^{-1/2} \ll 1)$

The Green's function for the acoustic field scattered by the elastic edge in time domain can be obtained by substituting the frequency domain result (B.2) from appendix B into (3.5),

$$G_s(\boldsymbol{x}, \boldsymbol{y}; t) = \frac{1}{2\pi^{\frac{3}{2}} c_0^{\frac{3}{2}}} \Phi(\boldsymbol{Y}) \frac{\sin \theta \sin \psi}{\epsilon^{\frac{1}{2}} x} D_t^{\frac{3}{2}} \delta(t_*), \tag{3.33}$$

where $\Phi(\mathbf{Y}) = Y^{\frac{1}{2}} \sin \frac{\theta}{2}$ is the velocity potential about the edge, the projection of \mathbf{y} onto the (y_1, y_2) -plane, and $Y = |\mathbf{Y}|$. This result is valid in the asymptotic limit $k\epsilon^{-1/2} \ll 1$, where ϵ is the intrinsic fluid loading parameter [18, 36, 39] that depends only on the properties of the structure and fluid (i.e., is frequency independent). By inspection, the total field $G_e = G_0 + G_s$ for the impermeable-elastic case can also be approximated by G_s in Eq. (3.33):

$$G_e(\boldsymbol{x}, \boldsymbol{y}; t) = \frac{1}{2\pi^{\frac{3}{2}}c^{\frac{3}{2}}} \Phi(\boldsymbol{Y}) \frac{\sin \theta \sin \psi}{\epsilon^{\frac{1}{2}}x} D_t^{\frac{3}{2}} \delta(t_*), \tag{3.34}$$

such that the pressure observed in the acoustic far field is

$$p(\boldsymbol{x},t) = \rho_0 D_t \iint \omega_3(\boldsymbol{y},\tau) F(\boldsymbol{x},\boldsymbol{Y}) D_t^{\frac{3}{2}} \delta(t_* - \tau) d\boldsymbol{y} d\tau,$$

$$= \rho_0 D_t^{\frac{5}{2}} \int \omega_3(\boldsymbol{y},t_r) F(\boldsymbol{x},\boldsymbol{Y}) d\boldsymbol{y}, \qquad (3.35)$$

where

$$F(\boldsymbol{x}, \boldsymbol{Y}) = \frac{1}{2\pi^{\frac{3}{2}}c^{\frac{3}{2}}} \frac{\sin\theta\sin\psi}{\epsilon^{\frac{1}{2}}x} \Psi(\boldsymbol{Y}). \tag{3.36}$$

Note that t_* has been replaced by $t_r = t - x/c$ in (3.17) for a compact turbulence source. Specific details on the compact vortex ring source and its trajectory are described in the following section.

B Vorticity distribution and vortex ring motion $(k\epsilon^{-1/2} \ll 1)$

Following the outline procedures by equations (3.19), (3.20), (3.21) and (3.23), the acoustic pressure expression for the impermeable-elastic case is

$$p\left(x, t + \frac{x}{c}\right) = \frac{\rho_0 \Gamma}{2\pi^{\frac{3}{2}} c^{\frac{3}{2}}} \frac{\sin \theta \sin \psi}{\epsilon^{\frac{1}{2}} x} D_t^{\frac{5}{2}} [\pi a^2 v_{\xi}(\mathbf{C})], \tag{3.37}$$

which enables an explicit determination of the temporal profile of the according acoustic pressure. The acoustic pressure is represented by the time derivative, of the (5/2)th order,

of the volume flux $\pi a^2 v_{\xi}$ through the vortex ring.

Recall that $D_t^{\frac{5}{2}}v_{\xi}(\mathbf{C}) = D_t^{\frac{1}{2}}[D_t^2v_{\xi}(\mathbf{C})]$, and $D_t^2v_{\xi}(\mathbf{C})$ may be derived in a dimensionless form (see derivation in appendix F),

$$D_{\bar{t}}^{2}v_{\xi}(\mathbf{C}) = -\frac{3}{8}U^{2}L^{-\frac{5}{2}}h(\bar{t}), \qquad (3.38)$$

where $\bar{t} = Ut/L$ is the dimensionless time, and

$$h\left(\overline{t}\right) = \overline{Y}^{-\frac{5}{2}} \sin\left(\frac{5}{2}\Theta - 3\alpha\right),\tag{3.39}$$

$$\overline{Y} = \frac{Y}{L} = \left(\overline{t}^2 + 1\right)^{\frac{1}{2}}, \quad \Theta = \tan^{-1}\left(\frac{\overline{t}\sin\alpha \mp \cos\alpha}{\overline{t}\cos\alpha \pm \sin\alpha}\right). \tag{3.40}$$

Here the time origin $\bar{t} = 0$ denotes the time instant when the vortex ring is at its nearest distance L to the edge.

Therefore, $D_{\overline{t}}^{\frac{5}{2}}v_{\xi}(\boldsymbol{C})$ in (3.37) may now be expressed as

$$D_{\bar{t}}^{\frac{5}{2}}[\pi a^{2}v_{n}(\mathbf{C})] = -\frac{3}{8}\pi a^{2}U^{\frac{5}{2}}L^{-3}D_{\bar{t}}^{\frac{1}{2}}[h(\bar{t})], \qquad (3.41)$$

and the substitution of (3.41), (3.39), and (3.40) into (3.37) yields the acoustic pressure,

$$p\left(\boldsymbol{x}, \overline{t} + \frac{x}{c_0}\right) = -\frac{3a^2 \rho_0 \Gamma U^{\frac{5}{2}}}{8\pi^{\frac{1}{2}} c_0^{\frac{3}{2}} L^3} \frac{\sin \theta \sin \psi}{\epsilon^{\frac{1}{2}} x} D_{\overline{t}}^{\frac{1}{2}} \left[h\left(\overline{t}\right) \right]. \tag{3.42}$$

3.2 Semi-infinite edge with non-uniform properties

In this section, the acoustic scattering of a turbulent eddy near a semi-infinite edge with non-uniform properties is considered. Due to the fundamental analytical challenge that the traditional Wiener-Hopf approach is well-suited for problems with discontinuous boundary condition but is unable to handle non-uniform edge conditions, we use a numerical approach to solve the corresponding acoustic problem for non-uniform edge properties. Also, due

to the technical challenge of modelling a semi-infinite plate in a numerical scheme using finite-length elements, the acoustic problem of a turbulent eddy (i.e., quadrupole) acoustic source near a finite plate setup is considered and presented in §3.2.1. This work employs a novel Mathieu function collation method of Colbrook & Priddin [14] described briefly in §3.2.2, which provides a general solution procedure for finite-length edge acoustic scattering problem with arbitrary boundary conditions. Section 3.2.3 solves the acoustic problem with particular kinematic boundary condition for a rigid porous edge.

3.2.1 Model problem

Consider the acoustic scattering problem of a quadrupole sound source close to the edge of a finite graded-porosity plate that lies in the region $-1 < x_1, y_1 \le +1, x_2, y_2 = 0,$ $-\infty < x_3, y_3 < \infty$ of the coincident Cartesian coordinate systems $\{(x_1, y_1), (x_2, y_2), (x_3, y_3)\}$ (see. figure 3.3), where lengths have been nondimensionalized by the semi-chord of the plate. The scattered field is denoted by ϕ with suppressed time factor $e^{-i\omega t}$ satisfies the Helmholtz equation

$$\left(k^2 + \nabla^2\right)\phi = 0. \tag{3.43}$$

The velocity potential ϕ_0 for a quadrupole sound source may be determined by

$$\phi_0(y_1, y_2) = \frac{ik^2}{4r_0^2} (y_1 - y_{1_0})(y_2 - y_{2_0}) H_2^{(1)}(kr_0), \tag{3.44}$$

where (y_{1_0}, y_{2_0}) is the quadrupole source location, $r_0(y_1, y_2) = \sqrt{(y_1 - y_{1_0})^2 + (y_2 - y_{2_0})^2}$ is the distance between the source and observer, and $H_n^{(1)}$ are Hankel functions of the first kind.

Note that large wavenumber k is used in current finite plate setup to minimize backscattering effects from the leading edge [50], and furnish an indirect comparison against the analytical semi-infinite plate setup.

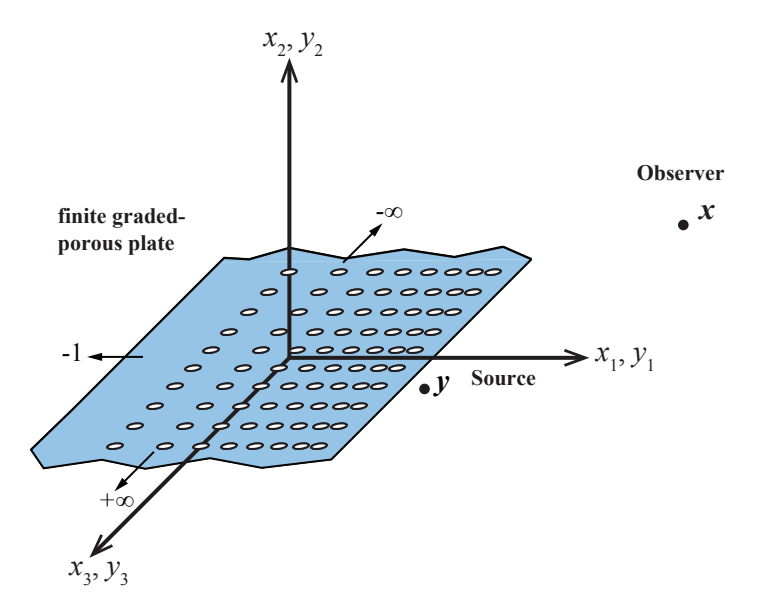


Figure 3.3: Schematic of the finite graded-porous plate and the coincident coordinate systems for the source $\mathbf{y} = (y_1, y_2, y_3)$ and the observer at $\mathbf{x} = (x_1, x_2, x_3)$.

3.2.2 Mathieu function collocation method

The Mathieu function collocation method of Colbrook & Priddin [14] introduces elliptic coordinates via $y_1 = \cosh \nu_1 \cos \nu_2$, $y_2 = \sinh \nu_1 \sin \nu_2$, where the appropriate domain becomes $\nu_1 \geq 0$ and $\nu_2 \in [0, \pi]$. The Helmholtz equation (3.43) along $|y_1| \geq 1$, $y_2 = 0$ and the scattered field at infinity become

$$\begin{cases} \frac{\cosh(2\nu_1) - \cos(2\nu_2)}{2} k^2 + \nabla^2_{\nu_1, \nu_2} \phi(\nu_1, \nu_2) = 0, \\ \phi|_{\nu_2 = 0} = \phi|_{\nu_2 = \pi} = 0, \\ \lim_{\nu_1 \to \infty} \nu_1^{1/2} \left(\frac{\partial}{\partial \nu_1} - ik \right) \phi(\nu_1, \nu_2) = 0. \end{cases}$$
(3.45)

Separation of variables for solutions of the form $V(\nu_1)W(\nu_2)$ leads to a regular Sturm-Liouville eigenvalue problem:

$$\begin{cases} W''(\nu_2) + (\lambda - \frac{k^2}{2}\cos(2\nu_2))W(\nu_2) = 0, \\ W(0) = W(\pi) = 0. \end{cases}$$
(3.46)

The solutions of (3.46) are sine-elliptic functions, denoted by

$$\operatorname{se}_{n}(\nu_{2}) = \sum_{l}^{\infty} B_{l}^{(n)} \sin(l\nu_{2}),$$
 (3.47)

where the Fourier series converges absolutely and uniformly on all compact sets of the complex plane [53], and the coefficients $B_l^{(n)}$ may be found via a simple approximation of Galerkin's method.

The corresponding $V(\nu_1)$ with the Sommerfeld condition at infinity are given by the Mathieu-Hankel functions

$$\operatorname{Hse}_{n}(\nu_{1}) = \operatorname{Jse}_{n}(\nu_{1}) + i\operatorname{Yse}_{n}(\nu_{1}). \tag{3.48}$$

These Mathieu-Hankel functions can be expanded in a series using Bessel functions [48, 53].

The full general solution of the acoustic scattering problem for any boundary condition on the finite thin plate can be written as

$$\phi(\nu_1, \nu_2) = \sum_{n=1}^{\infty} a_n \operatorname{se}_n(\nu_2) \operatorname{Hse}_n(\nu_1), \tag{3.49}$$

where a_n are unknown coefficients which must be determined by applying the appropriate boundary condition along the plate.

The far-field directivity $D(\theta)$ may be directly computed from the expansion of those Mathieu-Hankel functions (3.48). In the appropriate limit, ν_2 becomes the polar angle θ , and ν_1 becomes $\cosh^{-1} r$, which leads to

$$D(\theta) = \sqrt{\frac{2}{k\pi}} \sum_{n=1}^{\infty} \frac{a_n B_1^{(n)}}{C_n} \exp\left[\frac{(2p_n - 3)\pi}{4}i\right] \operatorname{se}_n(\theta).$$
 (3.50)

3.2.3 Kinematic boundary condition

The kinematic boundary condition at a non-uniform porous finite thin plate requires

$$\frac{\partial \phi}{\partial y_2} + \frac{\partial \phi_0}{\partial y_2} = \mu(y_1)[\phi](y_1), \tag{3.51}$$

where $[\phi](y_1) = (\phi(y_1, 0^+, y_3) - \phi(y_1, 0^-, y_3))$ denotes the velocity potential difference across the plate [28, 39]. Note that in §3.1, $\mu(y_1) = \mu = \alpha_H \overline{K}_R/R$ is a constant parameter that permits a uniformly-porous edge condition. To achieve a non-uniformly porous condition along the plate in current acoustic problem, it is straightforward to let μ vary along the chord, i.e., $\mu(y_1)$, which may be achieved through the variation of the pore aperture radius R, or the variation of open area ratio α_H , or a combination of varying both R and α_H . However, it is only the overall variation of $\mu(y_1)$ that truly matters in the model. Thus, we only let α_H vary along the chord rather than both variations of α_H and R, for simplicity.

The undetermined coefficient a_n is now determined in the expansion of (3.49) with the particular kinematic boundary condition (3.51). The approximate value of coefficients a_n is calculated by adopting a spectral collocation method [14], denoted by \tilde{a}_n .

Substitution of the general solution (3.49) truncates N terms into (3.51) yields,

$$\sum_{n=1}^{N} \widetilde{a}_n \operatorname{se}_n \left(\cos^{-1} y_1 \right) \left[1 - 2 \operatorname{Hse}_n(0) \mu(y_1) \sqrt{1 - y_1^2} \right] + \sqrt{1 - y_1^2} \frac{\partial \phi_0}{\partial y_2} = 0.$$
 (3.52)

Here \tilde{a}_n is evaluated at chosen Chebyshev points in Cartesian coordinates and equally-spaced collocation points in elliptic coordinates [4, 59], which is determined by

$$y_1 = \cos\left(\frac{2i-1}{2N}\pi\right), \quad i = 1, ..., N.$$
 (3.53)

The approximated coefficients \tilde{a}_n are now evaluated by solving an $N \times N$ linear system.

Chapter 4

Results

4.1 Uniformly-porous rigid edge

The acoustic power scalings on the vortex ring velocity U and the nearest distance of the vortex ring from the edge L depend on the value of m, which is a function of the dimensionless porosity parameter μ/k . Note that m must be evaluated numerically in general but may be determined analytically for special cases of low and high porosity limits. Complementary numerical analysis in appendix A demonstrates that the edge is effectively impermeable for $\mu/k < O(10^{-2})$, and achieves its high porosity limit for $\mu/k > O(10)$. Acoustic results for these two special cases and for the general case of arbitrary porosity value are provided in §4.1.1, 4.1.2, and 4.1.3, respectively. In §4.1.4, the experimental results from Applied Research Laboratory (ARL) at the Pennsylvania State University are briefly introduced.

4.1.1 Impermeable limit

The edge becomes effectively impermeable in the low porosity limit where μ/k is asymptotically small. By inspection of (A.9), it is easily found that $m = \frac{1}{2}$, n = 0, and

 $M(\psi,\theta) = \sqrt{2}\sin\frac{\theta}{2}(\sin\psi)^{\frac{1}{2}}$. In this case, (3.29) and (3.32) become:

$$p\left(x,\bar{t} + \frac{x}{c_0}\right) = \frac{\rho_0 \Gamma a^2 U^{\frac{3}{2}}}{4\sqrt{2}\pi^{\frac{1}{2}}c_0^{\frac{1}{2}}L^2} \frac{\sin\frac{\theta}{2}(\sin\psi)^{\frac{1}{2}}}{x} D_{\bar{t}}^{\frac{1}{2}} \left[g\left(\bar{t}\right)\right],\tag{4.1}$$

$$\Pi \propto U^5 L^{-4} \sin^2 \frac{\theta}{2},\tag{4.2}$$

which agree with the analytical solution of Kambe et al. [41] and recover the U^5 scaling law for radiated sound power and cardioid acoustic directivity of Ffowcs Williams & Hall [25]. Equation (4.1) obviates the acoustic pressure dependence on $D_{\bar{t}}^{\frac{1}{2}}\left[g\left(\bar{t}\right)\right]$ in the high porosity limit, i.e., is proportional to the time derivative of the $\frac{1}{2}$ th order of the volume flux through the vortex ring, which may be determined by [47]:

$$D_{\overline{t}}^{\frac{1}{2}}\left[g\left(\overline{t}\right)\right] = \int_{-\infty}^{t} \frac{\dot{g}(s)}{\pi(\overline{t}-s)^{\frac{1}{2}}} ds, \tag{4.3}$$

where $\dot{g}(s)$ represents the first time derivative of g(s).

Representative time histories of $g(\bar{t})$ and $\dot{g}(\bar{t})$ are provided in figure 4.1 for five rectilinear paths of the vortex ring past the porous edge, $\alpha = 0, -\pi/4, -\pi/2, -3\pi/4, -\pi$. Figure 4.1 (top left) together with (4.3) indicates that the acoustic pressure for each path changes rapidly near $\bar{t} = 0$, where the vortex ring passes closest to the edge. Note in figure 4.1 (top left) how the acoustic pressure amplitude is significantly affected in the impermeable rigid edge by the vortex path angle α .

4.1.2 High-porosity limit

The edge becomes acoustically transparent in the high porosity limit of asymptotically large μ/k values, where (A.9) provides $m=1, n=-\frac{1}{2}$, and $M(\psi,\theta)=\sin\theta\sin\psi$. The far-field acoustic pressure and acoustic power scaling behavior are:

$$p\left(\boldsymbol{x}, \overline{t} + \frac{x}{c_0}\right) = \frac{\rho_0 \Gamma a^2 U^2}{8\pi^{\frac{1}{2}} c_0 L^{\frac{5}{2}} \mu^{\frac{1}{2}}} \frac{\sin \theta \sin \psi}{x} D_{\overline{t}} \left[g\left(\overline{t}\right)\right], \tag{4.4}$$

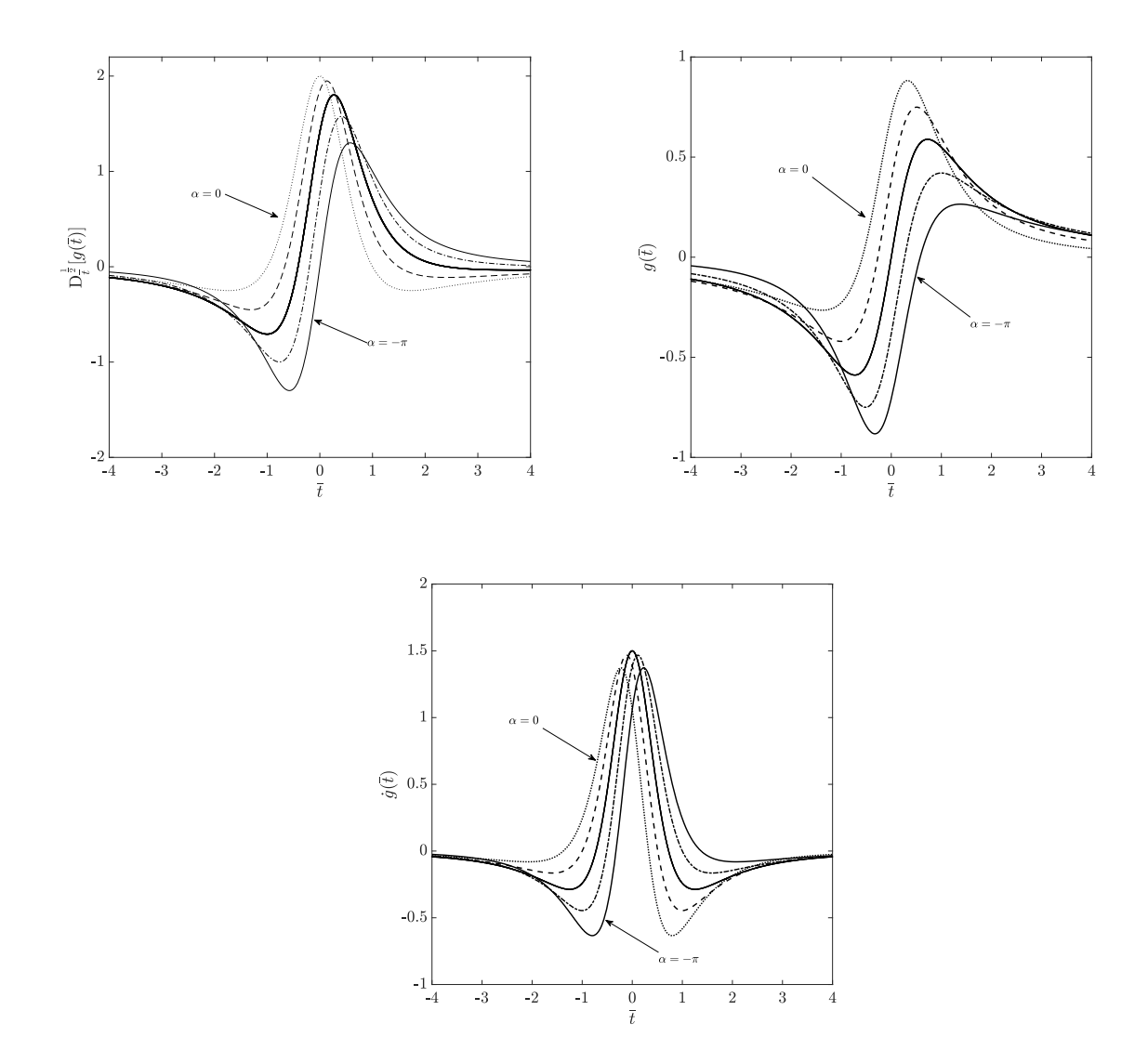


Figure 4.1: Time histories of acoustic pressure $D_{\overline{t}}^{\frac{1}{2}}\left[g\left(\overline{t}\right)\right]$ (top left), acceleration of volumetric flux through the vortex ring $g\left(\overline{t}\right)$ (top right) and $\dot{g}\left(\overline{t}\right)$ (bottom center) for the impermeable rigid edge. Results are plotted for vortex path angles $\alpha=0,-\pi/4,-\pi/2,-3\pi/4,-\pi$ relative to the rigid edge. The heavy line corresponds to $-\pi/2$. $D_{\overline{t}}^{\frac{1}{2}}\left[g\left(\overline{t}\right)\right]$ is the dimensionless acoustic pressure and shows an intermediate behavior between that of $g\left(\overline{t}\right)$ and $\dot{g}\left(\overline{t}\right)$.

$$\Pi \propto U^6 L^{-5} \sin^2 \theta,\tag{4.5}$$

which recovers the U^6 scaling law and the dipolar acoustic directivity $\sin^2 \theta$ by Jaworski & Peake [39]. Equation (4.4) obviates that the acoustic pressure in the high-porosity limit depends on $D_{\bar{t}}\left[g\left(\bar{t}\right)\right]$, i.e., is proportional to the acceleration of the fluid through the vortex ring:

$$D_{\overline{t}}\left[g\left(\overline{t}\right)\right] \equiv \dot{g}\left(\overline{t}\right) = -\frac{3}{2}\overline{Y}^{-\frac{5}{2}}\sin\left(\frac{5}{2}\Theta - 3\alpha\right),\tag{4.6}$$

which was determined by Chen & Jaworski [10].

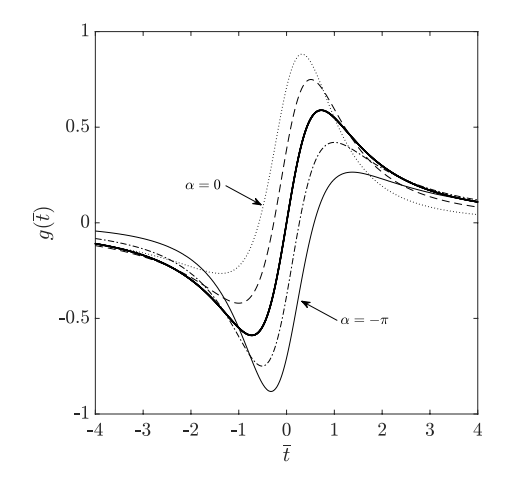
Representative time histories of $g(\bar{t})$ and $\dot{g}(\bar{t})$ are provided in figure 4.2 for five rectilinear paths of the vortex ring past the porous edge, $\alpha = 0, -\pi/4, -\pi/2, -3\pi/4, -\pi$. Figure 4.2 (right) together with (4.4) indicates that the acoustic pressure for each path changes rapidly near $\bar{t} = 0$, where the vortex ring passes closest to the edge. Note in figure 4.2 (right) how the acoustic pressure amplitude is weakly affected in the high-porosity limit by the vortex path angle α . Also, the acoustic waveform in the high porosity limit described by $\dot{g}(\bar{t})$ is symmetric (a 'W' shape) about $\bar{t} = 0$ for a vortex ring passing perpendicular to the plane of the edge, $\alpha = -\pi/2$.

4.1.3 General porosity case

The acoustic pressure solution (3.17) for arbitrary values of the dimensionless porosity parameter μ/k requires numerical evaluation. We now consider the case of arbitrary porosity effects, where the acoustic pressure is strictly determined by (3.29). The waveform of the acoustic pressure is directly determined by fractional derivative $D_{\bar{t}}^{m}\left[g\left(\bar{t}\right)\right]$, which can be evaluated in the Caputo sense [55]:

$$D_{\bar{t}}^{m} \left[g \left(\bar{t} \right) \right] = \frac{1}{2\pi} \int_{-\infty}^{+\infty} (-i\omega)^{m} \hat{g}(\omega) e^{-i\omega \bar{t}} d\omega,$$

$$= \frac{1}{\mathcal{G}(1-m)} \int_{-\infty}^{\bar{t}} \frac{\dot{g}(s)}{(\bar{t}-s)^{m}} ds. \tag{4.7}$$



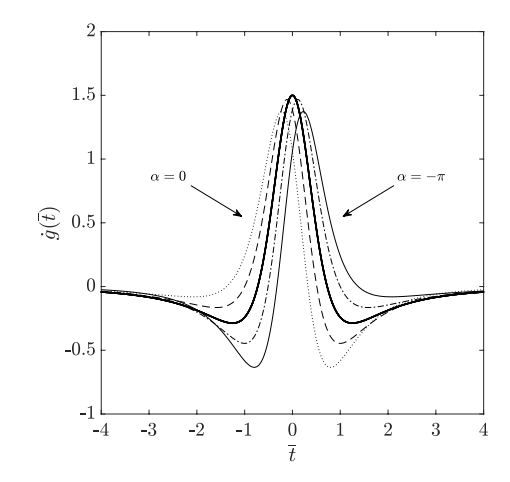
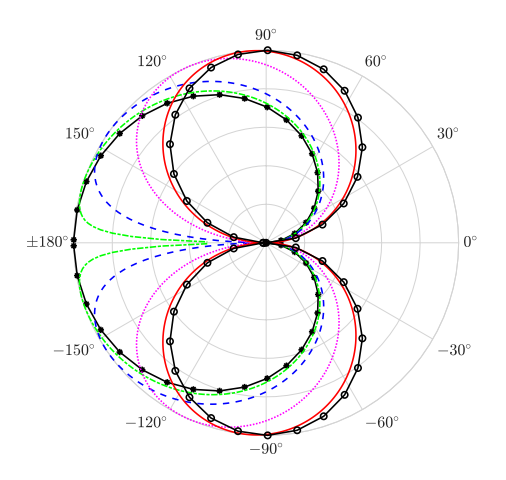


Figure 4.2: Time histories of volumetric flux through the vortex ring $g\left(\bar{t}\right)$ (left) and associated acoustic pressure $\dot{g}\left(\bar{t}\right)$ (right) in the limit of high porosity, $\mu/k\gg 1$. Results are plotted for vortex path angles $\alpha=0,-\pi/4,-\pi/2,-3\pi/4,-\pi$ relative to the porous edge. The heavy line corresponds to $-\pi/2$.

The full expression for $\dot{g}(s)$ is given in appendix B, and \mathcal{G} is the well-known gamma function. The value of parameter m for the leading solution term follows (A.11) and varies on the dimensionless porosity parameter μ/k , and this dependence is plotted in figure A.1 in appendix A.

Figure 4.3 plots the acoustic directivity and the corresponding time-dependent pressure waveforms of the noise emitted by a vortex ring passing near a semi-infinite porous edge, as a function of the dimensionless porosity parameter. appendix A details the evaluation of $M(\psi,\theta)$ for $\psi=\pi/2$. The transition of acoustic directivity from a cardioid to a dipole occurs smoothly with increasing values of the porosity parameter. Figure 4.3(b) illustrates how the asymmetric pressure waveform for impermeable edges found in §4.1.1 becomes increasingly symmetric as the porosity parameter increases, where the direction of the vortex ring relative to the porous edge affects the waveform shape.

The dependence of the acoustic power scalings γ and v on μ/k , readily obtained from (3.32) and (A.11), are illustrated in figure 4.4. Both exponent values vary monotonically between the formal asymptotic limits of low porosity ($\mu/k \ll 1$) and high porosity ($\mu/k \gg 1$). Figure 4.4 indicates that these limits may be refined by numerical computation, where the



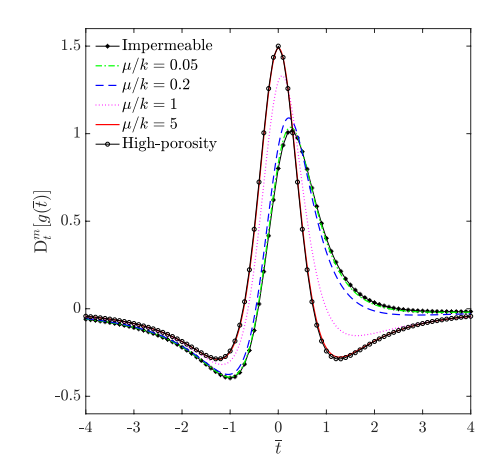


Figure 4.3: Acoustic directivity and corresponding acoustic pressure waveforms due to a vortex ring passing near a semi-infinite porous edge with various values and limits of the dimensionless porosity parameter μ/k . The vortex path angle is $\alpha = -\pi/2$. (a) Acoustic pressure directivity; (b) far-field pressure waveforms represented by $D_{\bar{t}}^m \left[g(\bar{t}) \right]$ in (4.7).

edge is effectively impermeable for $\mu/k < O(10^{-2})$ and the high-porosity limit is achieved for $\mu/k > O(10)$.

4.1.4 Comparison with experimental measurements from ARL

In this section, we briefly review the associated experiments conducted in ARL Penn State regarding the acoustic measurements of a vortex ring passing near an impermeable edge or a uniformly-porous rigid edge. A schematic of the experimental setup is presented in figure 4.5. A complete description of the experimental methods and measurement results to data are found in Yoas [60] where results are reproduced here with permission. The principal scaling and directivity results for a rigid, uniformly-porous edge are herein compared against out theoretical model predictions.

A Acoustic power scaling on vortex ring velocity

First, the effects of acoustic radiation power scaling with characteristic velocity U was measured and processed, where the comparison against present research is presented in figure 4.6. For the rigid impermeable edge ($\mu/k = 0$), measured acoustic power scales

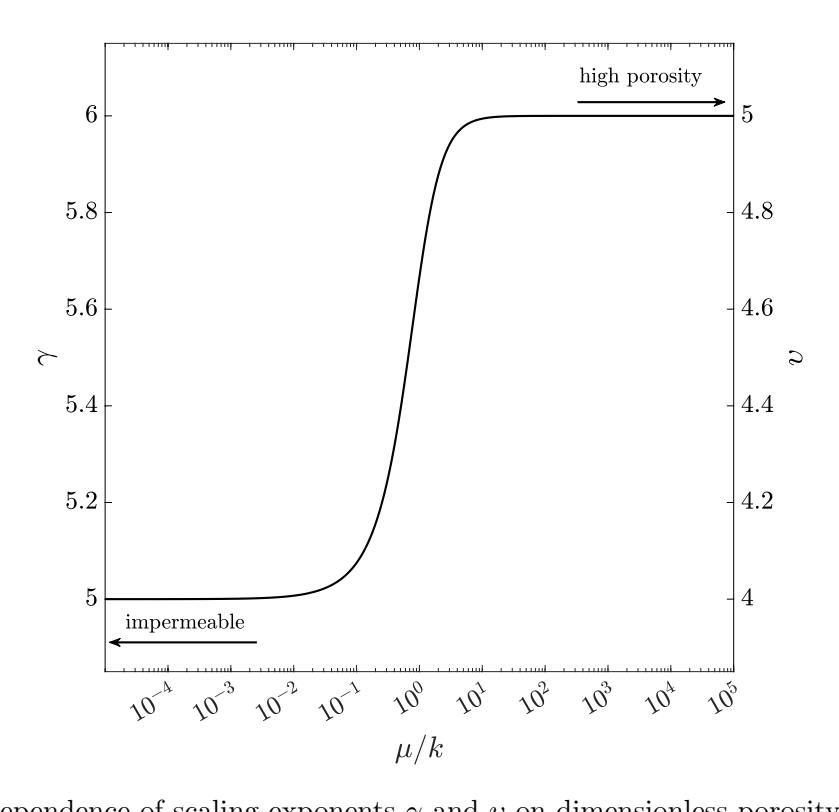
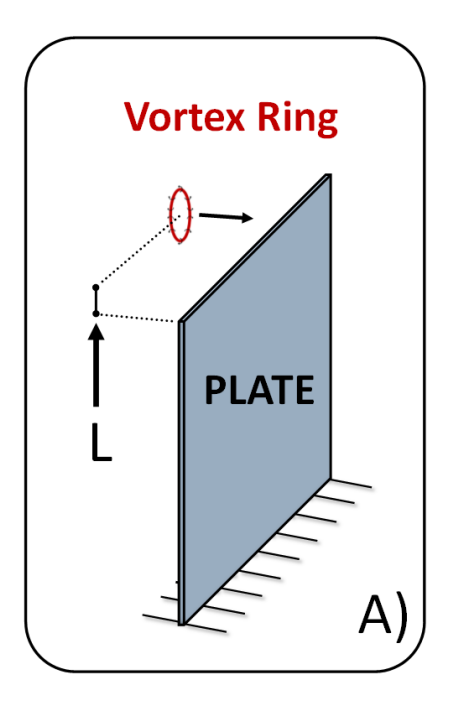


Figure 4.4: Dependence of scaling exponents γ and v on dimensionless porosity parameter μ/k . Acoustic power is proportional to $U^{\gamma}L^{-v}$.



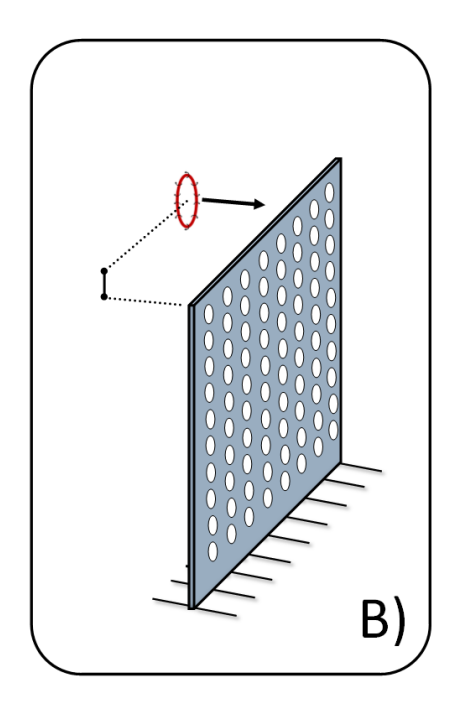


Figure 4.5: Schematic of a vortex ring convecting near a A) rigid impermeable plate and B) semi-infinite rigid plate with uniform porosity. Figure reproduced from Yoas [60, figure 2.3] with permission.

on the vortex ring speed as $U^{4.98}$, in close agreement with the theoretical prediction U^5 . As the porosity porosity parameter increases to $\mu/k = 0.49$, the acoustic power scales on $U^{5.32}$, as compared to the predicted $U^{5.39}$ in present work (cf. figure 4.4). For the high-porosity case ($\mu/k = 58.9$), the measured acoustic power scaling scales on $U^{5.99}$, which is also in excellent agreement with the theoretical prediction of U^6 . It is worth noting that the theoretical acoustic power scaling for intermediate value $\mu/k = 3.10$ is overpredicted as $U^{5.94}$ compared to the measured $U^{5.72}$, which needs further investigation. However, it is noted in this region that small changes to μ/k lead to large changes in the scaling exponent.

B Acoustic directivity

Second, the comparison of acoustic directivity between theoretical prediction in the present work and experimental measurements for the rigid impermeable edge and highly-porous edge are shown in figures 4.7 and 4.8, respectively. The directivity measurements

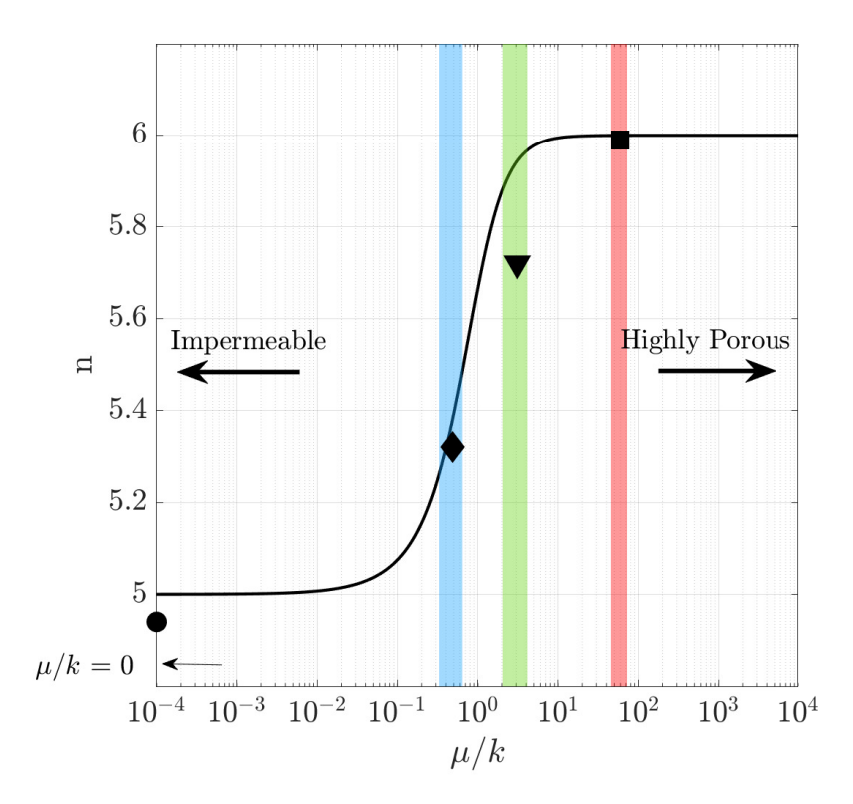


Figure 4.6: Comparison of predicted values of sound power law exponent n (solid line) to measurement (four markers with various symbols). The shaded regions blue, green, and red represent the μ/k ranges for $\mu/k=0.49$, $\mu/k=3.10$, $\mu/k=58.9$, respectively. The symbols indicate a) circle: $\mu/k=0$ and n=4.98, b) diamond: $\mu/k=0.49$ and n=5.32, c) triangle: $\mu/k=3.10$ and n=5.72, d) square: $\mu/k=58.9$ and n=5.99. Figure reproduced from Yoas [60, figure 4.4] with permission.

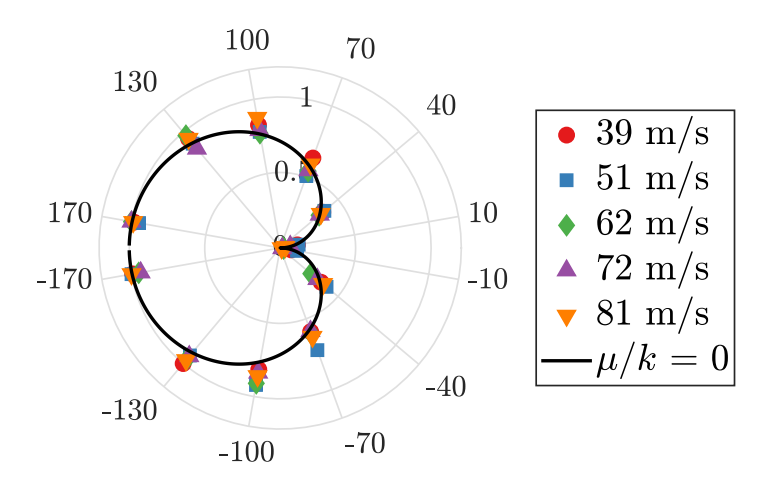


Figure 4.7: Impermeable rigid edge $(\mu/k=0)$: measured normalized acoustic directivity versus varying observation angle $\theta \in (-180^{\circ}, 180^{\circ})$ at different vortex ring speed. The solid line represents the cardioid pressure directivity $\sin \frac{\theta}{2}$ in (4.2). Figure reproduced from Yoas [60, figure 4.5 (a)] with permission.

of both two edge cases match well with their theoretical predictions in §§4.1.1 and 4.1.2. Additional acoustic directivity measurements at different dimensionless porosity parameter values (μ/k) are found in Yoas [60].

C Acoustic power scaling on vortex-edge distance

Third, the effect of acoustic power scaling with offset distance L between the vortex ring path and the edge is now discussed. Table 4.1 shows the acoustic power scaling exponents m at difference observation angles θ . For the impermeable edge $(\mu/k=0)$, the acoustic power exponent averaged across all angles shown in table 4.1(a) is $\overline{m}=-4.04$ (i.e., $L^{-4.04}$), which agrees closely with the predicted L^{-4} in (4.2). For the highly-porous edge $(\mu/k=58.9)$, the averaged acoustic power across all angles in table 4.1(b) scales as $\overline{m}=-4.94$ (i.e., $L^{-4.94}$), which is also close to the theoretical prediction of L^{-5} in (4.5). The reader might notice that different observation angles are selected for the calculation of the averaged acoustic power scaling exponent \overline{m} , which is due to the fact that the radiated noise decreases at angles close to the nulls. Thus, only data points with high acoustic signal-to-noise ratios are used.

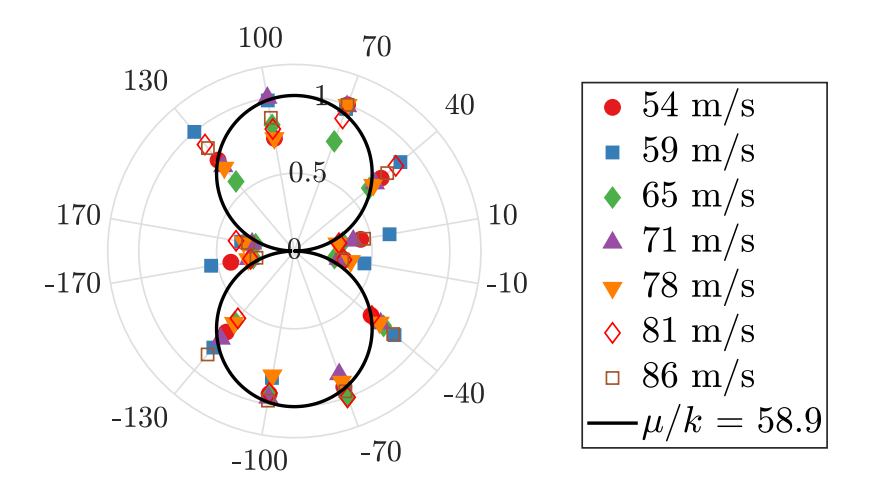


Figure 4.8: Highly-porous edge ($\mu/k = 58.9$): measured normalized acoustic directivity versus varying observation angle $\theta \in (-180^{\circ}, 180^{\circ})$ at different vortex ring speed. The solid line represents the predicted dipolar pressure directivity $\sin \theta$ in (4.5). Figure reproduced from Yoas [60, figure 4.5 (d)] with permission.

Table 4.1: Radiated acoustic power scaling as a function of offset distance L with selected varying observation angle θ : (a) $m_{\rm avg} = -4.04$ and (b) $m_{\rm avg} = -4.94$. (Yoas [60, table 4.2])

(a) Impermeable edge $(\mu/k = 0)$

(b) Highly-porous edge ($\mu/k = 58.9$)

θ	m	heta	m
-170	-4.21	-100	-4.8
-130	-3.92	-70	-4.9
130	-3.97	70	-5.0
170	-4.04	100	-4.9

D Temporal profile of acoustic pressure

Last, the results for the dimensionless waveforms of acoustic pressure in time are now discussed and compared. The temporal acoustic pressure waveform is estimated from microphone measurements using the following equations:

$$p_i(t) = \frac{1}{4\pi r_i} D_i(t - \frac{r_i}{c}) \beta(\theta_i), \qquad (4.8)$$

$$D_i(t) = \frac{4\pi r_i}{\beta(\theta_i)} p_i \left(t + \frac{r_i}{c} \right), \tag{4.9}$$

$$D_{\text{avg}}(t) = \frac{1}{N_{\text{mic}}} \sum_{i=1}^{N_{\text{mic}}} D_i(t), \qquad (4.10)$$

$$D = D_{\text{avg}}(t)/U^{n/2}, (4.11)$$

where $1/4\pi r_i$ accounts for spherical propagation of the sound wave, $D_i(t-r_i/c)$ is the acoustic source strength, and $\beta(\theta_i)$ is the directivity pattern of the acoustic pressure $(\sin(\theta/2))$ for a rigid impermeable edge, $\sin\theta$ for a highly-porous edge). The subscripts i refers to different angular position of the microphone. Note that the temporal pressure waveforms at different values of dimensionless porosity parameter μ/k in present work are determined by (4.7), which is different from the nondimensionalization process in experiments using (4.11). Thus, the shapes of temporal pressure waveforms for different porosity parameter values is the primary concern here.

Figure 4.9 shows the temporal pressure waveform for the rigid impermeable edge ($\mu/k = 0$). The acoustic pressure increases monotonically with time and reaches the peak at time $\tau = 0$ due to the strong vortex-edge interaction as the vortex ring approaches the edge. After the edge encounter, the pressure decays with time as the vortex ring moves away from the edge. The waveforms elongate with decreasing vortex ring speed, which may be associated to the longer interaction time between the vortex ring and edge. The source waveforms at different vortex ring speeds overlap into a shape that agrees with the theoretical prediction of the temporal acoustic pressure profile in figure 4.3.

Figure 4.10 shows the temporal pressure waveform for the highly-porous edge ($\mu/k = 58.9$). The acoustic pressure increases monotonically with time and reaches the peak at

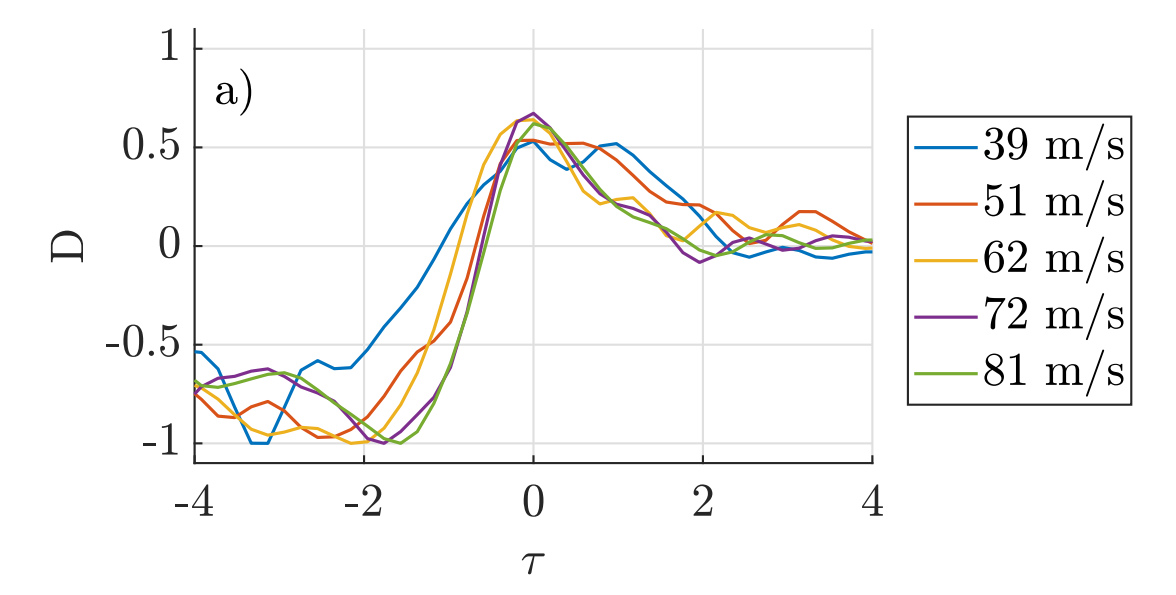


Figure 4.9: Impermeable rigid edge ($\mu/k = 0$): measured dimensionless pressure waveforms D at different vortex ring speed. Figure reproduced from Yoas [60, figure 4.7 (a)] with permission.

time $\tau=0$ due to the strong vortex-edge interaction as the vortex ring approaches the edge. After the edge encounters, the pressure decays decays with time as vortex ring moves far away from the edge. Similar to the results in figure 4.9, elongated waveforms are also observed at smaller vortex ring speeds due to the longer interaction time between the vortex ring and edge. It is worth noting that the pressure waveforms at different vortex ring speeds overlap into a 'W' shape, which agree with the theoretical prediction of temporal acoustic pressure profile in figure 4.3.

4.2 Impermeable elastic edge

Similarly, this section seeks to find the acoustic power scalings on the vortex ring velocity U and the nearest distance of the vortex ring from an impermeable elastic edge L, which is valid for small k in the sense that $k\epsilon^{-1/2} \ll 1$. Acoustic results for this special asymptotic limit are provided in the following section.

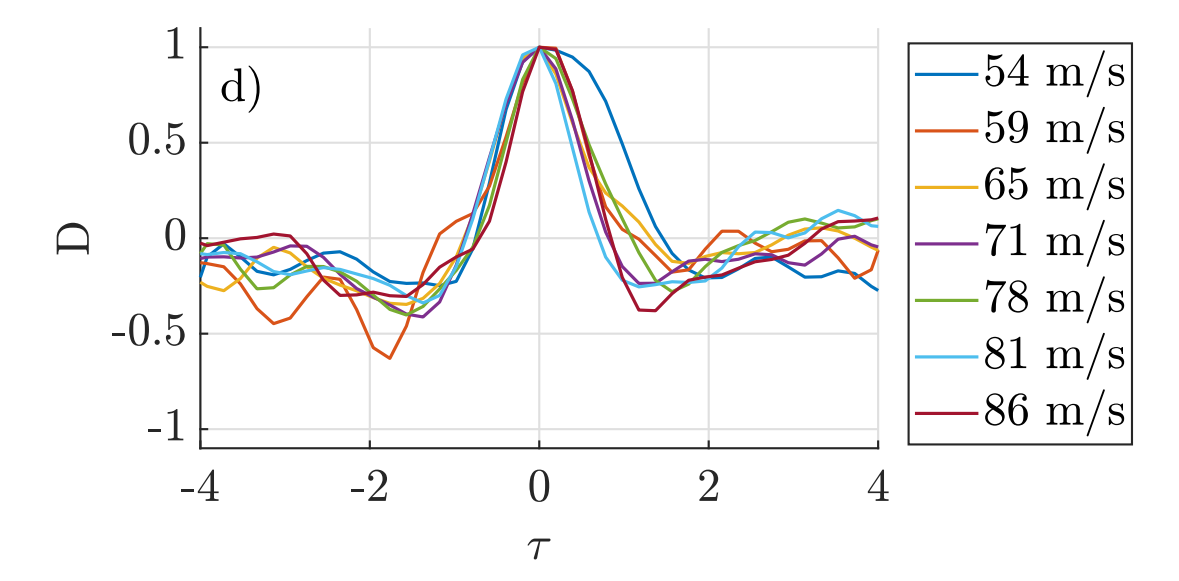


Figure 4.10: Highly-porous edge ($\mu/k = 58.9$): measured dimensionless pressure waveforms D at different vortex ring speed. Figure reproduced from Yoas [60, figure 4.7 (d)] with permission.

4.2.1 Asymptotic limit $k\epsilon^{-1/2} \ll 1$

The scaling law and directivity of radiated acoustic power for a vortex ring passing near an impermeable elastic edge are now determined. From (3.30), it is a straightforward matter to find that the corresponding far-field acoustic pressure radiated by a vortex ring passing near an impermeable-elastic edge ($k\epsilon^{-1/2} \ll 1$) becomes like

$$p \propto U^{\frac{7}{2}}L^{-3},$$
 (4.12)

and the corresponding acoustic power Π is

$$\Pi = \frac{p^2}{\rho_0 c_0} \propto U^7 L^{-6}. \tag{4.13}$$

The directivity has the same $\sin \theta$ dependence as that of the edge case with high porosity identified in (4.5).

As is shown in (3.41), the temporal profile of the acoustic pressure is represented by $D_{\bar{t}}^{\frac{5}{2}}v_{\xi}(C)$, which has been rearranged in the form of $D_{\bar{t}}^{\frac{1}{2}}\left[m\left(\bar{t}\right)\right]$. The purpose of this refor-

mulation is that we may now use the definition of the (1/2)th derivative of $m(\bar{t})$ directly,

$$D_{\overline{t}}^{\frac{1}{2}}\left[h\left(\overline{t}\right)\right] = \frac{1}{2\pi} \int_{-\infty}^{+\infty} \left(-i\omega\right)^{\frac{1}{2}} \hat{h}(\omega) e^{-i\omega t} d\omega = \int_{-\infty}^{t} \frac{\dot{h}(s)}{\left[\pi(\overline{t}-s)\right]^{\frac{1}{2}}} ds, \tag{4.14}$$

where the derivation can be found in [47]. This relation was previously adapted by Kambe et al. [41] for the acoustic problem of a rigid edge interacts with a vortex ring. Note that (4.14) may also be derived from (4.7) when m = 1/2.

Representative time histories of $D_{\bar{t}}^{\frac{1}{2}}\left[h\left(\bar{t}\right)\right]$, $h\left(\bar{t}\right)$ and $\dot{h}\left(\bar{t}\right)$ are provided in figure 4.11 for five rectilinear paths of the vortex ring past the porous edges, $\alpha=0,-\pi/4,-\pi/2,-3\pi/4,-\pi$. Figure 4.11 (top left) together with (3.42) indicates that the acoustic pressure for each path changes rapidly near $\bar{t}=0$, where the vortex ring passes closest to the edge. Note in figure 4.11 (top left) how the acoustic pressure amplitude is weakly affected in the given asymptotic limit by the vortex path angle α .

It is worth noting that Kambe *et al.* [41] identified a symmetric acoustic pressure signal (proportional to $D_{\bar{t}}^{\frac{1}{2}}\left[h\left(\bar{t}\right)\right]$) for a rigid, impermeable edge when $\alpha=0$. However, the temporal curves of acoustic pressure profile shown in figure 4.2 (left) and 4.11 (top left) show that symmetric pressure signals occur for vortex path angles $\alpha=-\pi/2$ and $\alpha=-\pi$ for the high-porosity case and the specific asymptotic limit of the elastic case, respectively.

4.3 Semi-infinite edge with non-uniform properties

In this section, we discuss the results of present edge-noise problem with non-uniform edge conditions. A special case with uniform-porosity is first considered numerically and compared against previous analytical results to furnish a numerical verification in section 4.3.1. Section 4.3.2 discusses the effects of non-uniform porosity on the corresponding acoustic results.

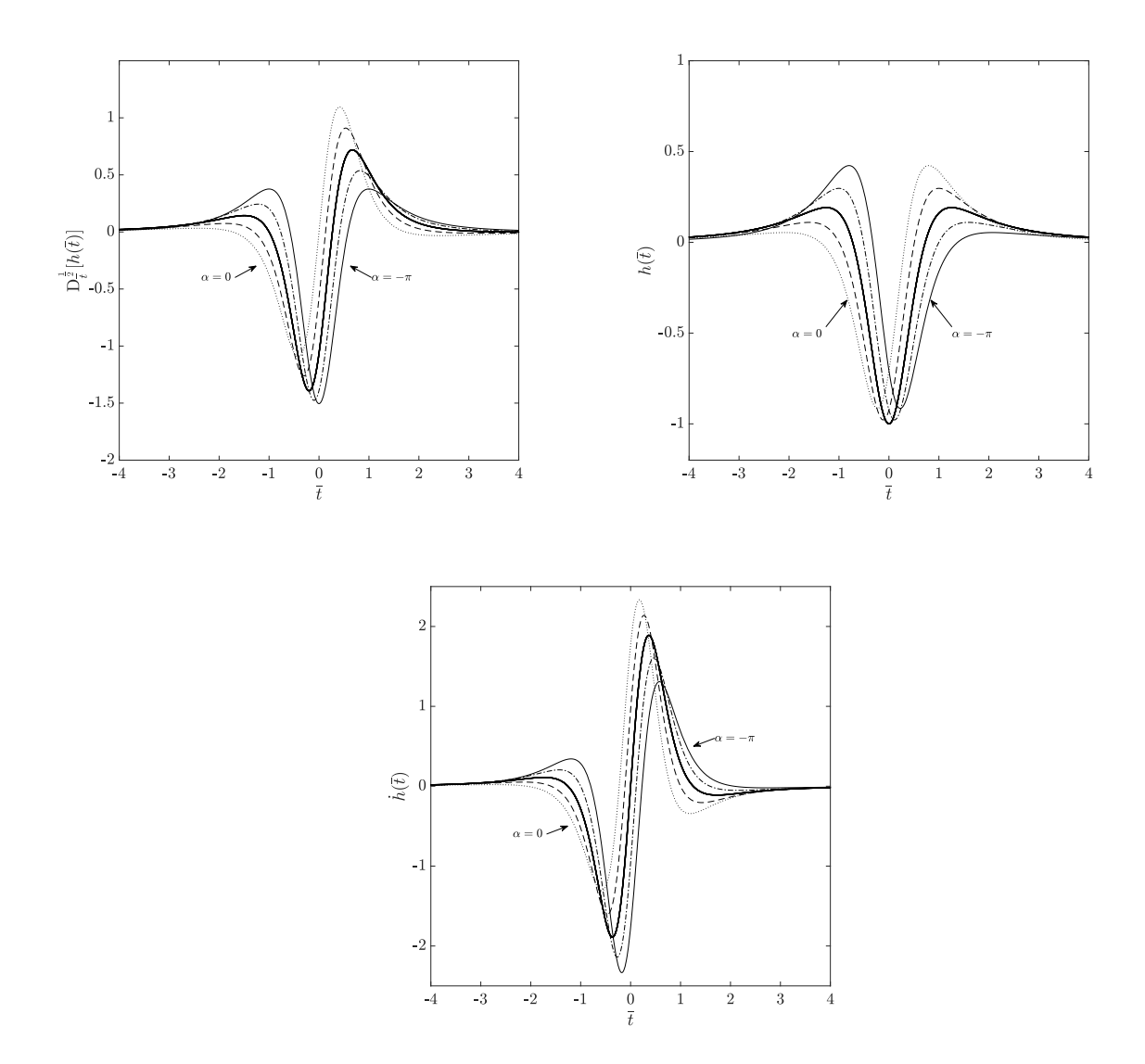


Figure 4.11: Time histories of acoustic pressure $D_{\overline{t}}^{\frac{1}{2}}\left[h\left(\overline{t}\right)\right]$ (top left), acceleration of volumetric flux through the vortex ring $h\left(\overline{t}\right)$ (top right) and $\dot{h}\left(\overline{t}\right)$ (bottom center) in the limit of $k\epsilon^{-1/2}\ll 1$. Results are plotted for vortex path angles $\alpha=0,-\pi/4,-\pi/2,-3\pi/4,-\pi$ relative to the porous edge. The heavy line corresponds to $-\pi/2$. $D_{\overline{t}}^{\frac{1}{2}}\left[h\left(\overline{t}\right)\right]$ is the dimensionless acoustic pressure and shows an intermediate behavior between that of $h\left(\overline{t}\right)$ and $\dot{h}\left(\overline{t}\right)$.

Table 4.2: Different values of porosity μ/k calculated from different values of fractional open area α_H and wavenumber k, and a constant pore radius R.

k	R	α_H	μ/k
100	0.001	0.005π	0.2
100	0.001	0.025π	1
100	0.001	0.125π	5

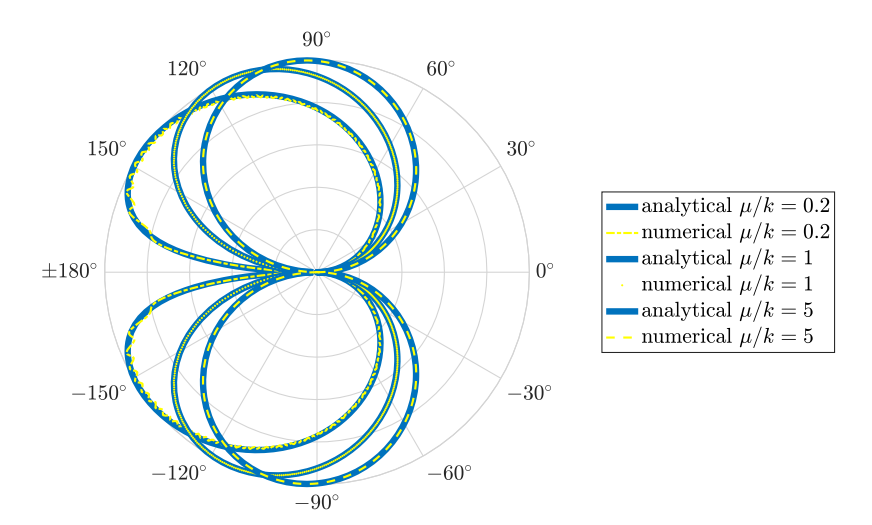


Figure 4.12: Comparison of acoustic directivity for analytical solution based on Wiener-Hopf technique and numerical solution based on Mathieu function collocation method with various values and limits of the dimensionless porosity parameter μ/k .

4.3.1 Numerical verification for uniformly-porous rigid edge

In this section, we explore the numerical performance of the Mathieu function collocation method with constant porosity parameter μ/k , and compared the numerical results with the theoretical predictions in §4.1.

Figure 4.12 shows the comparison of acoustic directivity for the analytical results in figure 4.3 and the Mathieu function collocation method, where different values of porosity parameter μ/k are used and shown in table 4.2. The source location is fixed at (1,0.0001) near the edge of the plate. To guarantee a non-compact (i.e., localized) source region near the trailing edge of the plate (to minimize the effect of the leading edge), the wavenumber k is set to 100 and the radius of the pore is set to 0.001.

Table 4.3: Averaged values of graded porosity μ/k calculated from different values of fractional open area at trailing edge α_T and constant pore radius R and wavenumber k.

k	R	α_L	α_T	$(\mu/k)_{avg}$
100	0.001	0	0.005π	0.1
100	0.001	0	0.025π	0.5
100	0.001	0	0.125π	2.5

4.3.2 Graded porous rigid edge

This section investigates the effect of the nonuniform distributions of porosity on trailingedge noise. Graded porosity along a flat plate is now considered through the mathematical expression

$$\alpha_H(y_1) = \alpha_L + \frac{(\alpha_T - \alpha_L)}{2}(x+1),$$
(4.15)

where α_L and α_T are the open area ratios at the leading and trailing edge, respectively. We consider a graded porosity distribution along the plate where porosity increases linearly from the leading edge to the trailing edge, where $\alpha_L \leq \alpha_T$ hold for all cases. Hold fixed are the wavenumber k, source location, and dimensionless pore radius are used as that in §4.3.1 unless otherwise specified. Consider three nonuniform cases with the same open area ratio at the leading edge $\alpha_L = 0$, and with three different open area ratio at the trailing edge $\alpha_T = 0.005\pi, 0.025\pi$ and 0.125π , the averaged values of the porosity distribution value along the plate may also be calculated, and are indicated in table 4.3. The graded porosity cases have the same α_T as that of the uniform cases to furnish a direct comparison.

Figure 4.13 plots and compares the far-field acoustic directivities with different values of porosity parameter μ/k between the uniform and nonuniform (graded) porosity cases at high frequency (k = 100), where the backscattering effects from the leading edge may be largely minimized, and the plate is considered to be non-compact. First, figure 4.13 shows that the far-field acoustic directivity magnitude decreases from low porosity to high porosity for the uniform and graded porosity cases, respectively, which validates the effects of porosity

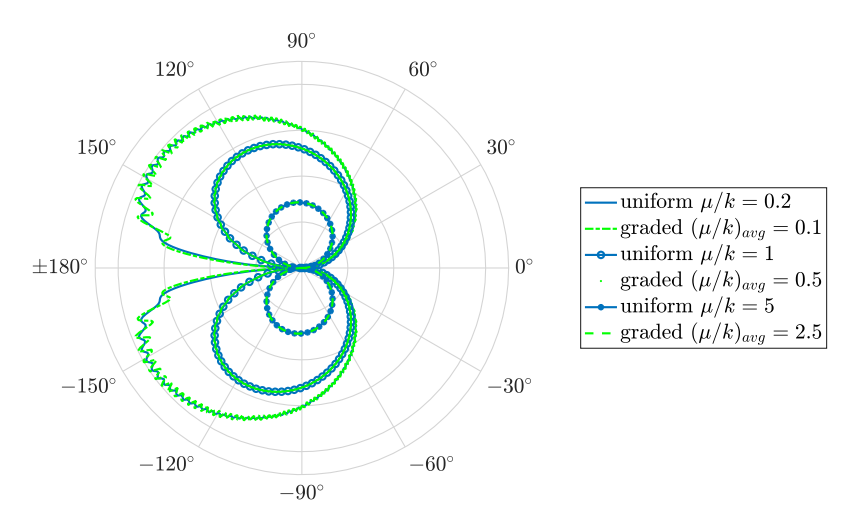


Figure 4.13: Comparison of the acoustic pressure field (not normalized) for uniformly porosity and nonuniform porosity cases, where the nonuniform cases consider graded porosity distribution along the plate with the same open area ratios at the trailing edge α_T as the uniform case

in noise reduction. Second, figure 4.13 also shows that the far-field acoustic directivity patterns for uniform and graded porosity cases overlap at the same porosity parameter μ/k at the trailing edge, regardless of whether the leading edge of the plate has zero porosity or not, which indicates that only the local porosity parameter value at the trailing edge dominates the acoustic directivity. It is worth noting that the acoustic directivity pattern becomes more modulated at the low porosity value for the graded porosity case when the leading edge is rigid ($\alpha_L = 0$), as compared to the uniform porosity case where the leading edge has the same porosity value as trailing edge ($\alpha_L = \alpha_T$). This modulated behavior of acoustic directivity may be due to backscattering effects [50] from the rigid leading edge, which still exist at high frequency but may be mitigated by increasing the porosity at the leading edge, as shown in figure 4.13.

Figure 4.14 plots and compares the far-field acoustic directivities with different values of porosity parameter μ/k between two different frequency regimes, k=20 and k=100. Similar to the case with k=100, the far-field acoustic directivity magnitude at k=20 decreases from low porosity to high porosity. For the acoustic directivity results at k=20, the cardioid or dipolar shape holds at low or high dimensionless porosity parameter μ/k , thus

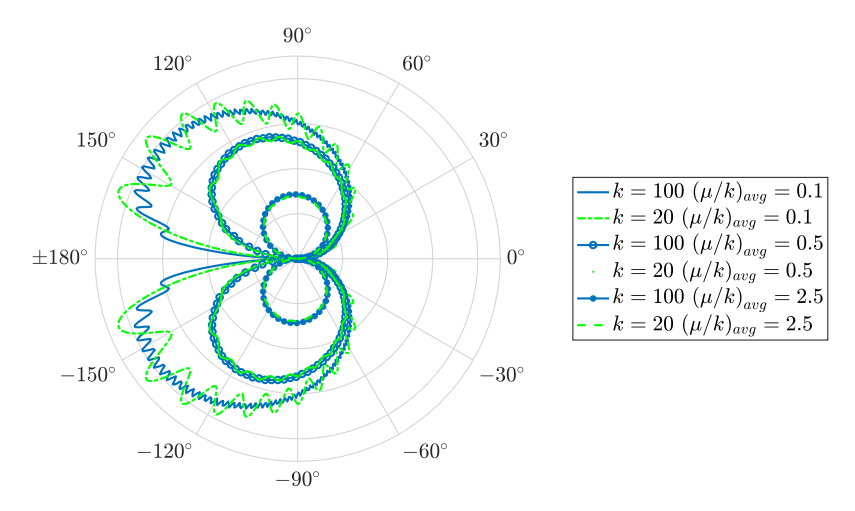


Figure 4.14: Comparison of unnormalized acoustic directivity for the graded porosity cases with different values of dimensionless porosity parameter μ/k at k=20 and k=100

the plate is still considered to be semi-infinite. It is also shown that the acoustic directivity patterns still overlap at medium or high porosity parameter value μ/k at a relatively smaller frequency (k=20). However, increased modulation of the acoustic directivity is observed at k=20 at small porosity parameter value (μ/k) compared to the result at k=100.

In all, the present verification of the numerical scheme of Colbrook & Priddin [14] using a finite-length plate in the appropriate parametric limits of a semi-infinite edge support the further exploration of realistic porosity designs for target noise reduction and/or directivity.

Chapter 5

Conclusions

An analytical framework is developed in the time domain to estimate the sound in the acoustic far-field resulting from a vortex ring passing near a rigid-porous or an impermeable-elastic edge with uniform properties. We adapt the work of Kambe *et al.* [41] for an impermeable-rigid edge condition, which permits a parametric check and direct comparisons on this analysis of different edge conditions. The time-domain Green's functions for the porous and elastic cases are developed in this work by extending the vortex-ring analysis procedure by Kambe *et al.* [41] and integrating with it the asymptotic results for turbulence edge scattering for poroelastic plates by Jaworski & Peake [39].

In contrast to the U^5 acoustic power scaling law and cardioid directivity for turbulence and vortex sources near a rigid half plane, the present analysis identifies a U^6 scaling in a highly-porosity limit ($\mu/k \gg 1$) and a U^7 scaling for an elastic case under a specific limit of fluid loading condition ($k\epsilon^{-1/2} \ll 1$) in agreement with the scattering analysis for poroelastic edges by Jaworski & Peak [39]. Both cases yield a dipolar directivity of acoustic pressure, $\sin \theta_0$. Furthermore, new scalings on the minimum distance of the vortex ring from the edges are established, where L^{-5} and L^{-6} dependencies occur for the porous and elastic cases, respectively. The time-dependent component of the scattered field depends strongly on the orientation of the vortex path relative to the edge, where the particular impermeable, porous, and elastic cases examined each yield symmetric waveforms along different vortex-

ring paths. The time-dependent waveforms and accompanying scaling trends of acoustic power on both the vortex ring speed U and offset distance from the edge L establish a basis for experimental validation of poroelastic-edge noise suppression in particular parametric limits.

The acoustic emission by a turbulent eddy source near a semi-infinite edge with graded porosity is then studied numerically using Mathieu function collocation approach of Colbrook & Priddin [14] adapted for the current trailing-edge noise model problem. We compare the numerical results of the acoustic directivity with the analytical predictions of vortex-edge model problem, and find close agreement across different values of dimensionless porosity parameter μ/k , in addition to the modulated directivity pattern at low porosity (small μ/k) that are expected by the backscattering effect by the plate leading edge. Furthermore, we study the effects of a graded porosity distribution on the acoustic directivity, where the graded porosity is modeled in the format of increasing porosity from the plate leading edge to the trailing edge. We compare the acoustic directivity results with that of uniform porosity cases and find no significant difference at high frequency (k = 100), as only the local porosity parameter value at the trailing edge influences the acoustic results. This finding holds even at relatively-low frequency (k=20) for the edges with medium to high average porosity parameter values across the chord. However, increased modulation of the acoustic directivity pattern occurs at k=20 for the edge with a lower porosity average value compared to that at k = 100, which is likely due to the increasing strong backscattering effect of the leading edge.

Appendix A

Green's function for a uniformly-porous edge

Application of the Fourier inversion formula (3.5) to (3.3) yields

$$(\nabla^2 + k^2) \, \widehat{G}_{rp}(\boldsymbol{x}, \boldsymbol{y}; k) = \delta(\boldsymbol{x} - \boldsymbol{y}), \tag{A.1}$$

where $k = \omega/c_0$ is the wavenumber and ω is the angular frequency. $\boldsymbol{x} = (x_1, x_2, x_3)$ and $\boldsymbol{y} = (y_1, y_2, y_3)$ represent the positions of the observer and the source, respectively.

By appeal to the reciprocal theorem [57], the positions of observer and source may be interchanged without modifying the Green's function, i.e., $\widehat{G}_{rp}(\boldsymbol{x}, \boldsymbol{y}; k) = \widehat{G}_{rp}(\boldsymbol{y}, \boldsymbol{x}; k)$. Therefore, the Green's function may be expressed as:

$$\widehat{G}_{rp}(\boldsymbol{x}, \boldsymbol{y}; k) = \widehat{G}_0(\boldsymbol{y}, \boldsymbol{x}; k) + \widehat{G}_s(\boldsymbol{y}, \boldsymbol{x}; k), \tag{A.2}$$

where $\widehat{G}_0(\boldsymbol{y}, \boldsymbol{x}; k)$ is the incident spherical wave generated by point source \boldsymbol{x} in free space,

$$\widehat{G}_0(\boldsymbol{y}, \boldsymbol{x}; k) = -\frac{1}{4\pi |\boldsymbol{x} - \boldsymbol{y}|} e^{ik|\boldsymbol{x} - \boldsymbol{y}|}, \tag{A.3}$$

and $\widehat{G}_s(\boldsymbol{x},\boldsymbol{y};k)$ is the scattered solution due to the interaction of the incident field \widehat{G}_0 and

the solid body (edge). At large distances of the source from the edge, where $x = |x| \to \infty$, \hat{G}_0 can be expressed asymptotically as

$$\widehat{G}_0(x, y; k) \sim A \exp[-ik(\widehat{x}_1 y_1 + \widehat{x}_2 y_2)],$$
 (A.4)

where

$$A = -\frac{1}{4\pi x} \exp(ikx - ik\hat{x}_3 y_3), \tag{A.5}$$

and the direction of the source x is denoted by

$$\hat{\boldsymbol{x}} = \boldsymbol{x}/x = (\hat{x}_1, \hat{x}_2, \hat{x}_3),$$

$$\hat{x}_1 = \sin \psi_0 \cos \theta_0, \quad \hat{x}_2 = \sin \psi_0 \sin \theta_0, \quad \hat{x}_3 = \cos \psi_0.$$

From the result of the scattered field for a porous edge by Jaworski & Peake [39], the corresponding Green's function for the scattered field may be determined:

$$\widehat{G}_s(\boldsymbol{y}, \boldsymbol{x}; k) = -\frac{1}{2} i Y^{\frac{1}{2}} \pi^{-\frac{3}{2}} B \sin \frac{\theta}{2} \frac{\exp \left[ikx - ik\cos\psi_0 y_3 + \frac{\pi}{4}i \right]}{x} \quad \text{as } Y \to 0,$$
 (A.6)

where $Y = (y_1^2 + y_2^2)^{\frac{1}{2}}$ is the projection of \boldsymbol{y} on the (y_1, y_2) -plane. Here B is a variable that depends on the wavenumber k, the properties of the porous edge, and the directivity of the incident field:

$$B = \frac{k \sin \psi_0 \sin \theta_0}{K_+(k \sin \psi_0 \cos \theta_0)},\tag{A.7}$$

where $K_{+}(k \sin \psi_0 \cos \theta_0)$ is the 'plus' function of the associated Wiener-Hopf kernel $K(\alpha)$ after multiplicative factorization, denoted $K_{+}(\alpha)$ by Jaworski & Peake [39, (4.12)].

The kernel function $K(\alpha)$ can be rewritten as $K(\alpha) = (\alpha + k)^{1/2}(\alpha - k)^{1/2}J(\alpha)$, where $(\alpha \pm k)^{1/2}$ are regular in the upper/lower half planes of complex variable α and $J(\alpha) \to 1$

as $|\alpha| \to \infty$. Therefore,

$$K_{+}(\alpha) = (\alpha + k)^{1/2} J_{+}(\alpha),$$

where

$$J_{+}(\alpha) = \exp\left[\frac{1}{2\pi i} \int_{\mathcal{C}} \frac{\log J(\xi)}{\xi - \alpha} d\xi\right]. \tag{A.8}$$

The integration contour \mathcal{C} is chosen and extend from $-\infty$ to $+\infty$ on the real axis to avoid the branch cuts from $\pm k$ to $\pm k \pm i\infty$. Note that $K_+(\alpha)$ must be determined numerically, but may be evaluated asymptotically in the limits of low or high edge porosity. At this point the reciprocal theorem is evolved to revert to the original source-observer configuration, which removes the subscripts on the angular positions. The analytical expressions for Bhave been determined by Jaworski & Peake [39] for two asymptotic limits of low and high effective porosity:

$$B \sim \begin{cases} (2k)^{1/2} \sin \frac{\theta}{2} (\sin \psi)^{1/2}, & \mu/k \ll 1, \\ \mu^{-1/2} k \sin \theta \sin \psi, & \mu/k \gg 1, \end{cases}$$
 (A.9)

where $\mu/k = \alpha_H \overline{K}_R/kR$ is the dimensionless porosity parameter.

For the purpose of investigating acoustic pressure directivity and scaling behaviors, it is convenient to express B as

$$B = M(\psi, \theta) k^m \mu^n, \tag{A.10}$$

where m and n are the exponents of the wavenumber k and the parameter $\mu = \alpha_H \overline{K}_R/R$ composed of porosity of the half plane, respectively, as described in detail in Section 3.1.2.A. The far-field directivity in this reciprocal problem for the scattered field follows from evaluating $M(\psi, \theta)$ for fixed ψ and varying θ from $-\pi$ to π . Note that both $M(\psi, \theta)$ and m vary with the porosity parameter μ , and must be determined numerically in general.

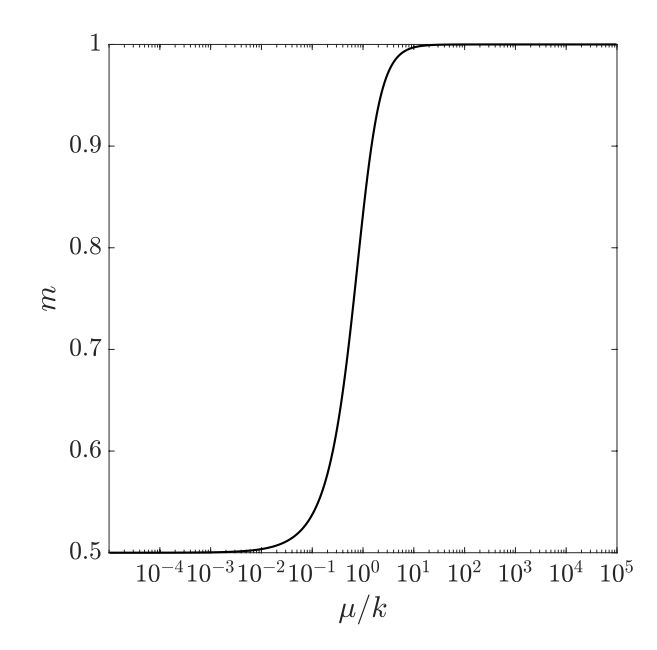


Figure A.1: Dependence of wavenumber parameter m on the dimensionless porosity parameter μ/k .

Equations (A.7) and (A.10) permit m to be computed as

$$m = 1 - \frac{\partial \log[K_{+}(k\cos\theta)]}{\partial \log k},\tag{A.11}$$

for $\psi = \pi/2$ and $\mu = 1$. Figure A.1 plots the dependence of m on μ/k for $\theta = \pi/4$, whose value does not affect these results.

Appendix B

Green's function for an uniformly-elastic edge

For the impermeable-elastic case $(k\epsilon^{-1/2} \ll 1, \ \epsilon = \rho_0 k/(m_p k_B^2))$, the variable B in (A.6) can be simplified as

$$B_e = \frac{k \sin \psi_0 \sin \theta_0}{K_+(k \sin \psi_0 \cos \theta_0)} \sim \frac{k^{\frac{3}{2}} \sin \psi \sin \theta}{\epsilon^{\frac{1}{2}}},$$
 (B.1)

where the subscripts on the angular positions are reverted to the original source-observer configuration, and ϵ is the intrinsic fluid loading parameter [18, 36, 39] that depends only on the properties of the structure and fluid, m_p is the plate mass, and k_B is the *in vacuo* bending wavenumber.

By substitution of (B.1) into (A.6), the scattered field for the impermeable-elastic case can be represented by

$$\widehat{G}_{s}(\boldsymbol{y}, \boldsymbol{x}; k) = \frac{1}{2} i Y^{\frac{1}{2}} (\pi c_{0})^{-\frac{3}{2}} Y^{\frac{1}{2}} \sin \frac{\theta}{2} \frac{\sin \psi_{0} \sin \theta_{0}}{\epsilon^{\frac{1}{2}} x} (-i\omega)^{\frac{3}{2}} \exp (ikx - iky_{3} \cos \psi_{0}), \quad (B.2)$$

where $Y = (y_1^2 + y_2^2)^{\frac{1}{2}}$ is the projection of \boldsymbol{y} on the (y_1, y_2) -plane, and $\omega = ck$.

Appendix C

First derivative of the temporal function of acoustic pressure, $\dot{g}(s)$

Equations (3.26) and (3.27) yield,

$$g(s) = (s^{2} + 1)^{-\frac{3}{4}} \sin\left[\frac{3}{2} \tan^{-1}\left(\frac{s \sin \alpha \mp \cos \alpha}{s \cos \alpha \pm \sin \alpha}\right) - 2\alpha\right]. \tag{C.1}$$

The first derivative of g(s) is obtained by direct application of the chain rule,

$$\dot{g}(s) = -\frac{3}{2}s(s^2 + 1)^{-\frac{7}{4}}\sin\left[\frac{3}{2}\tan^{-1}\left(\frac{s\sin\alpha \mp \cos\alpha}{s\cos\alpha \pm \sin\alpha}\right) - 2\alpha\right]$$
$$\pm \frac{3}{2}(s^2 + 1)^{-\frac{7}{4}}\cos\left[\frac{3}{2}\tan^{-1}\left(\frac{s\sin\alpha \mp \cos\alpha}{s\cos\alpha \pm \sin\alpha}\right) - 2\alpha\right],\tag{C.2}$$

where the upper sign holds for $0 \le \alpha \le \pi$, and the lower sign holds for $-\pi \le \alpha \le 0$. Note that (C.2) is used for the evaluation of integral in (4.7) and is equivalent to (4.6).

Appendix D

Estimate of vortex-edge interaction time

Kambe et al. [41, figure 6] and Yoas [60, figure 4.1] indicate experimentally that the path of a vortex ring near a porous edge is not perfectly rectilinear due to its hydrodynamic interaction with the edge, where the change in path becomes more pronounced with increasing vortex ring speed (or circulation, cf. (3.30)). Figure D.1 illustrates an idealisation of the modified path, where the vortex ring approaches along a straight path, turns by angle β toward the edge along a circular arc of radius L, and leaves along a different straight path. The model developed in §2 for a single rectilinear vortex ring path is justified if the duration of time over which the path turns is small relative to the period of the acoustic waveform.

Here it is conservatively assumed that the vortex ring maintains the same speed U in the circular arc as is does on the rectilinear segments. The dimensionless traverse time of the vortex ring in the arc segment may be estimated as

$$\bar{t}_a = \frac{Ut_a}{a} = \frac{L}{a}\beta,\tag{D.1}$$

where $t_a = (L\beta)/U$, β is the turning angle of the vortex path, and a is the radius of the

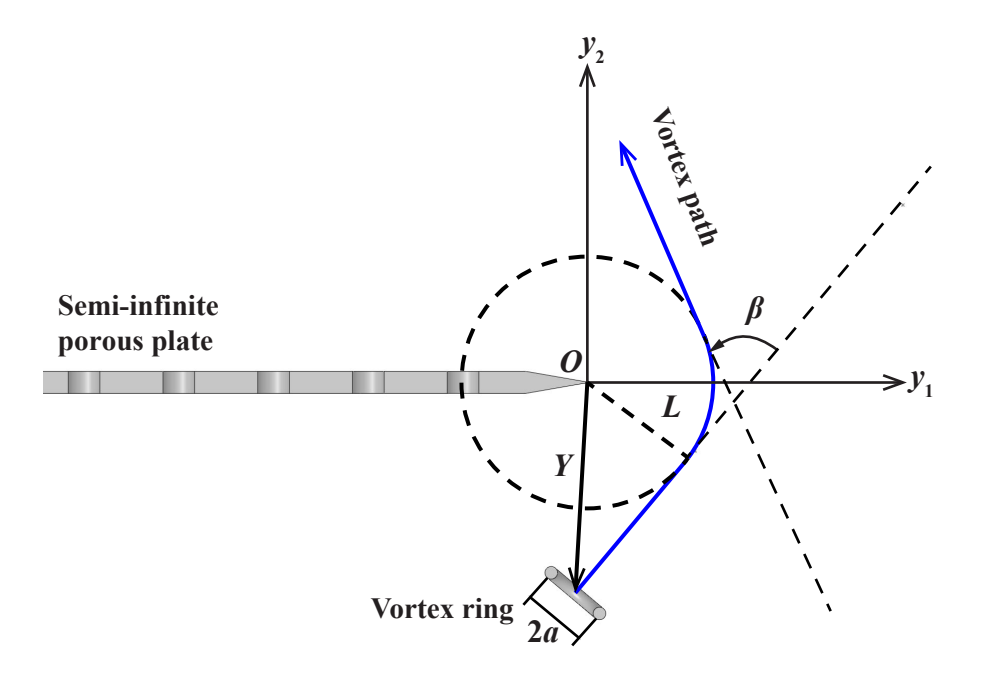


Figure D.1: Schematic of a vortex ring path (blue) affected by hydrodynamic interactions with a semi-infinite porous edge. The vortex path is idealized as three continuous segments: two rectilinear segments and one circular arc with a radius of L. The turning angle of the vortex path is denoted as β .

vortex ring. In [60], L = 9.8 mm and a = 6.5 mm, and the maximum value of the turning angle β is approximately 13.3°. Furthermore, figure 4.3(b) suggests a dimensionless acoustic waveform period of approximately 8. Therefore, the ratio of the vortex-edge interaction time and the effective period of the waveform is approximately $\bar{t}_a/8 = 4.4\%$. Therefore, the influence of the path turning due to the vortex-edge interaction on the entire pressure waveform is marginal and may be neglected in the present work.

Appendix E

Analyticity of the proposed stream function

Given the velocity potential $\Phi(\boldsymbol{Y})=Y^{\frac{1}{2}}\sin\frac{\theta_0}{2}$, supposing that the stream function is $\Psi(\boldsymbol{Y})=-Y^{\frac{1}{2}}\cos\frac{\theta_0}{2}$, the Cauchy-Riemann equations in (3.13) must be satisfied, where $Y=|\boldsymbol{Y}|=(y_1^2+y_2^2)^{\frac{1}{2}}$ and $\theta_0=\tan^{-1}\frac{y_2}{y_1}$.

$$\frac{\partial}{\partial y_1} \Phi(\mathbf{Y}) = \frac{\partial}{\partial y_1} \left((y_1^2 + y_2^2)^{\frac{1}{4}} \sin \frac{\tan^{-1} \frac{y_2}{y_1}}{2} \right)
= \frac{1}{2} (y_1^2 + y_2^2)^{-\frac{3}{4}} \sin \frac{\tan^{-1} \frac{y_2}{y_1}}{2} y_1 - (y_1^2 + y_2^2)^{\frac{1}{4}} \frac{1}{2} \cos \frac{\tan^{-1} \frac{y_2}{y_1}}{2} \left(\frac{y_2}{y_1^2} \right) \frac{y_1^2}{y_1^2 + y_2^2}
= \frac{1}{2} (y_1^2 + y_2^2)^{-\frac{3}{4}} \left(y_1 \sin \frac{\tan^{-1} \frac{y_2}{y_1}}{2} - y_2 \cos \frac{\tan^{-1} \frac{y_2}{y_1}}{2} \right)$$
(E.1)

$$\frac{\partial}{\partial y_2} \Phi(\mathbf{Y}) = \frac{\partial}{\partial y_2} \left((y_1^2 + y_2^2)^{\frac{1}{4}} \sin \frac{\tan^{-1} \frac{y_2}{y_1}}{2} \right)
= \frac{1}{2} (y_1^2 + y_2^2)^{-\frac{3}{4}} \sin \frac{\tan^{-1} \frac{y_2}{y_1}}{2} y_2 + (y_1^2 + y_2^2)^{\frac{1}{4}} \frac{1}{2} \cos \frac{\tan^{-1} \frac{y_2}{y_1}}{2} \left(\frac{1}{y_1} \right) \frac{y_1^2}{y_1^2 + y_2^2}
= \frac{1}{2} (y_1^2 + y_2^2)^{-\frac{3}{4}} \left(y_1 \cos \frac{\tan^{-1} \frac{y_2}{y_1}}{2} + y_2 \sin \frac{\tan^{-1} \frac{y_2}{y_1}}{2} \right)$$
(E.2)

$$\frac{\partial}{\partial y_1} \Psi(\mathbf{Y}) = \frac{\partial}{\partial y_1} \left(-(y_1^2 + y_2^2)^{\frac{1}{4}} \cos \frac{\tan^{-1} \frac{y_2}{y_1}}{2} \right)
= -\frac{1}{2} (y_1^2 + y_2^2)^{-\frac{3}{4}} \cos \frac{\tan^{-1} \frac{y_2}{y_1}}{2} y_1 - (y_1^2 + y_2^2)^{\frac{1}{4}} \frac{1}{2} \sin \frac{\tan^{-1} \frac{y_2}{y_1}}{2} \left(\frac{y_2}{y_1^2} \right) \frac{y_1^2}{y_1^2 + y_2^2}
= -\frac{1}{2} (y_1^2 + y_2^2)^{-\frac{3}{4}} \left(y_1 \cos \frac{\tan^{-1} \frac{y_2}{y_1}}{2} + y_2 \sin \frac{\tan^{-1} \frac{y_2}{y_1}}{2} \right)$$
(E.3)

$$\frac{\partial}{\partial y_2} \Psi(\mathbf{Y}) = \frac{\partial}{\partial y_2} \left(-(y_1^2 + y_2^2)^{\frac{1}{4}} \cos \frac{\tan^{-1} \frac{y_2}{y_1}}{2} \right)
= -\frac{1}{2} (y_1^2 + y_2^2)^{-\frac{3}{4}} \cos \frac{\tan^{-1} \frac{y_2}{y_1}}{2} y_2 + (y_1^2 + y_2^2)^{\frac{1}{4}} \frac{1}{2} \sin \frac{\tan^{-1} \frac{y_2}{y_1}}{2} \left(\frac{1}{y_1} \right) \frac{y_1^2}{y_1^2 + y_2^2}
= \frac{1}{2} (y_1^2 + y_2^2)^{-\frac{3}{4}} \left(y_1 \sin \frac{\tan^{-1} \frac{y_2}{y_1}}{2} - y_2 \cos \frac{\tan^{-1} \frac{y_2}{y_1}}{2} \right)$$
(E.4)

It is easy to find by examining (E.1) and (E.3), (E.2) and (E.4) that,

$$\frac{\partial}{\partial y_1} \Phi(\mathbf{Y}) = \frac{\partial}{\partial y_2} \Psi(\mathbf{Y}), \tag{E.5}$$

$$\frac{\partial}{\partial y_2} \Phi(\mathbf{Y}) = -\frac{\partial}{\partial y_1} \Psi(\mathbf{Y}). \tag{E.6}$$

Therefore, Cauchy-Riemann equations in (3.13) are given for the velocity potential $\Phi(\mathbf{Y})$ and stream function $\Psi(\mathbf{Y})$.

Appendix F

Derivations of derivatives of vortex ring speed: $\mathbf{D}_{\overline{t}}v_{\xi}(\mathbf{C})$ and $\mathbf{D}_{\overline{t}}^{2}v_{\xi}(\mathbf{C})$

Suppose that the vortex ring moves rectilinearly with velocity Ue, where e is a unit vector with components $(\cos \alpha, \sin \alpha)$ in the (y_1, y_2) -plane (cf. figure 3.2) and the vortex path is sufficiently distant from the edge (L > a). This assumption of the rectilinear vortex motion has been shown to be valid by Kambe $et\ al.$ [41] for the sound problem of a vortex ring near an impermeable-rigid plane.

From (3.23) we notice

$$v_{\xi}(\mathbf{C}) = \frac{\partial}{\partial \xi} \Phi(\mathbf{C})$$

$$= (0,1) \cdot (\frac{\partial}{\partial \eta}, \frac{\partial}{\partial \xi}) \Phi(\mathbf{C})$$

$$= (\mathbf{e} \cdot \nabla) \Phi(\mathbf{C})$$
(F.1)

Therefore the first derivative of $v_{\xi}(\mathbf{C})$ is

$$D_{t}v_{\xi}(\mathbf{C}) = v_{\xi}(\mathbf{C}) \cdot \nabla v_{\xi}(\mathbf{C})$$

$$= U\mathbf{e} \cdot \nabla v_{\xi}(\mathbf{C})$$

$$= U(\mathbf{e} \cdot \nabla)^{2} \Phi(\mathbf{C})$$

$$= U(\mathbf{e} \cdot \nabla)^{2} \Phi(\mathbf{Y}). \tag{F.2}$$

It is convenient to introduce the complex variable $z=y_1+\mathrm{i}y_2=Y\mathrm{e}^{\mathrm{i}\Theta}$, where the complex potential function $f=\Phi(\boldsymbol{Y})+\mathrm{i}\Psi(\boldsymbol{Y})=-\mathrm{i}z^{\frac{1}{2}}$. Since

$$v_{\xi}(\mathbf{C}) = \text{Re}\left\{e^{\mathrm{i}\alpha}\frac{\mathrm{d}f}{\mathrm{d}z}\right\},$$
 (F.3)

therefore,

$$v_{\xi}(C) = \operatorname{Re}\left\{e^{i\alpha}(-i)\frac{1}{2}z^{-\frac{1}{2}}\right\}$$

$$= \operatorname{Re}\left\{e^{i\alpha}(-i)\frac{1}{2}Y^{-\frac{1}{2}}e^{-i\frac{1}{2}\Theta}\right\}$$

$$= \operatorname{Re}\left\{-\frac{1}{2}Y^{-\frac{1}{2}}\sin\left(\frac{1}{2}\Theta - \alpha\right) - i\frac{1}{2}Y^{-\frac{1}{2}}\sin\left(\frac{1}{2}\Theta - \alpha\right)\right\}$$

$$= -\frac{1}{2}Y^{-\frac{1}{2}}\sin\left(\frac{1}{2}\Theta - \alpha\right), \tag{F.4}$$

and

$$(e \cdot \nabla)^{2} \Phi(\mathbf{Y}) = \operatorname{Re} \left\{ e^{i2\alpha} \frac{d^{2}f}{dz^{2}} \right\}$$

$$= \operatorname{Re} \left\{ e^{i2\alpha} (-i) (-\frac{1}{4}) z^{-\frac{3}{2}} \right\}$$

$$= \operatorname{Re} \left\{ e^{i2\alpha} (-i) (-\frac{1}{4}) Y^{-\frac{3}{2}} e^{-i\frac{3}{2}\Theta} \right\}$$

$$= \operatorname{Re} \left\{ i\frac{1}{4} Y^{-\frac{3}{2}} \cos\left(2\alpha - \frac{3}{2}\Theta\right) + \frac{1}{4} Y^{-\frac{3}{2}} \sin\left(\frac{3}{2}\Theta - 2\alpha\right) \right\}$$

$$= \frac{1}{4} Y^{-\frac{3}{2}} \sin\left(\frac{3}{2}\Theta - 2\alpha\right). \tag{F.5}$$

Therefore,

$$D_t v_{\xi}(\mathbf{C}) = \frac{1}{4} U Y^{-\frac{3}{2}} \sin\left(\frac{3}{2}\Theta - 2\alpha\right),\tag{F.6}$$

Let the time origin to be the instant when the vortex ring is nearest to the edge with the distance Y = L. The vortex position at time t can then be represented by

$$(Y\cos\Theta, Y\sin\Theta) = (Ut\cos\alpha \pm L\sin\alpha, Ut\sin\alpha \mp L\cos\alpha),$$
 (F.7)

where the upper sign holds for $0 \le \alpha \le \pi$, and the lower sign holds for $0 \ge \alpha \ge -\pi$.

From (F.7), we get

$$Y = \sqrt{Y^2 \cos^2 \Theta + Y^2 \sin^2 \Theta}$$

$$= \sqrt{(Ut \cos \alpha \pm L \sin \alpha)^2 + (Ut \sin \alpha \mp L \cos \alpha)^2}$$

$$= \sqrt{U^2 t^2 + L^2}$$

$$= L(\bar{t}^2 + 1)^{\frac{1}{2}}, \qquad (F.8)$$

and

$$\Theta = \tan^{-1} \left(\frac{Ut \sin \alpha \mp L \cos \alpha}{Ut \cos \alpha \pm L \sin \alpha} \right)$$
$$= \tan^{-1} \left(\frac{\bar{t} \sin \alpha \mp \cos \alpha}{\bar{t} \cos \alpha \pm \sin \alpha} \right), \tag{F.9}$$

where $\bar{t} = Ut/L$ is defined as the dimensionless time.

Equation (F.6) now may be rearranged in dimensionless form,

$$D_{\overline{t}}v_{\xi}(C) = \frac{1}{4}UY^{-\frac{3}{2}}\sin\left(\frac{3}{2}\Theta - 2\alpha\right)$$

$$= \frac{1}{4}UL^{-\frac{3}{2}}\left(\overline{t}^{2} + 1\right)^{-\frac{3}{4}}\sin\left(\frac{3}{2}\Theta - 2\alpha\right)$$

$$= \frac{1}{4}UL^{-\frac{3}{2}}g\left(\overline{t}\right), \tag{F.10}$$

where

$$g\left(\overline{t}\right) = \overline{Y}^{-\frac{3}{2}} \sin\left(\frac{3}{2}\Theta - 2\alpha\right), \quad \overline{Y} = \frac{Y}{L} = \left(\overline{t}^2 + 1\right)^{\frac{1}{2}}.$$
 (F.11)

The second derivative of $v_{\xi}(C)$ is now determined from (F.2),

$$D_t^2 v_{\xi}(\mathbf{C}) = v_{\xi}(\mathbf{C}) \cdot \nabla D_t v_{\xi}(\mathbf{C})$$
$$= U^2 (\mathbf{e} \cdot \nabla)^3 \Phi(\mathbf{Y}), \tag{F.12}$$

and

$$(e \cdot \nabla)^{3} \Phi(\mathbf{Y}) = \operatorname{Re} \left\{ e^{i3\alpha} \frac{d^{3} f}{dz^{3}} \right\}$$

$$= \operatorname{Re} \left\{ e^{i3\alpha} (-i) \left(\frac{3}{8} \right) z^{-\frac{5}{2}} \right\}$$

$$= \operatorname{Re} \left\{ e^{i3\alpha} (-i) \left(\frac{3}{8} \right) Y^{-\frac{5}{2}} e^{-i\frac{5}{2}\Theta} \right\}$$

$$= \operatorname{Re} \left\{ i \left(-\frac{3}{8} \right) Y^{-\frac{5}{2}} \cos \left(3\alpha - \frac{5}{2}\Theta \right) + \frac{3}{8} Y^{-\frac{5}{2}} \sin \left(3\alpha - \frac{5}{2}\Theta \right) \right\}$$

$$= -\frac{3}{8} Y^{-\frac{5}{2}} \sin \left(\frac{5}{2}\Theta - 3\alpha \right). \tag{F.13}$$

Therefore,

$$D_t^2 v_{\xi}(\mathbf{C}) = -\frac{3}{8} U^2 Y^{-\frac{5}{2}} \sin\left(\frac{5}{2}\Theta - 3\alpha\right),\tag{F.14}$$

which may also be rearranged non-dimensionally,

$$D_{\bar{t}}^{2} v_{\xi}(\mathbf{C}) = -\frac{3}{8} U^{2} Y^{-\frac{5}{2}} \sin\left(\frac{5}{2}\Theta - 3\alpha\right)$$

$$= -\frac{3}{8} U^{2} L^{-\frac{5}{2}} \left(\bar{t}^{2} + 1\right)^{-\frac{5}{4}} \sin\left(\frac{5}{2}\Theta - 3\alpha\right)$$

$$= -\frac{3}{8} U^{2} L^{-\frac{5}{2}} m\left(\bar{t}\right), \tag{F.15}$$

where

$$m\left(\overline{t}\right) = \overline{Y}^{-\frac{5}{2}} \sin\left(\frac{5}{2}\Theta - 3\alpha\right), \quad \overline{Y} = \frac{Y}{L} = \left(\overline{t}^2 + 1\right)^{\frac{1}{2}}.$$
 (F.16)

Bibliography

- [1] I. D. Abrahams. Scattering of sound by a heavily loaded finite elastic plate. *Proceedings* of the Royal Society of London A, 378(1772):89–117, 1981.
- [2] I. D. Abrahams. Scattering of sound by an elastic plate with flow. *Journal of Sound and Vibration*, 89(2):213–231, 1983.
- [3] L. J. Ayton. Acoustic scattering by a finite rigid plate with a poroelastic extension.

 Journal of Fluid Mechanics, 791:414–438, 2016.
- [4] J. Boyd. Chebyshev and Fourier spectral methods, courier corporation, 2001.
- [5] T. F. Brooks and T. H. Hodgson. Trailing edge noise prediction from measured surface pressures. *Journal of Sound and Vibration*, 78(1):69–117, 1981.
- [6] P. A. Cannell. Edge scattering of aerodynamic sound by a lightly loaded elastic halfplane. *Proceedings of the Royal Society of London A*, 347(1649):213–238, 1975.
- [7] P. A. Cannell. Acoustic edge scattering by a heavily loaded elastic half-plane. *Proceedings of the Royal Society of London A*, 350(1660):71–89, 1976.
- [8] A. V. G. Cavalieri, W. R. Wolf, and J. W. Jaworski. Numerical solution of acoustic scattering by finite perforated elastic plates. *Proceedings of the Royal Society of London* A, 472(2188):20150767, 2016.
- [9] H. Chen and J. Jaworski. Noise generation by a vortex ring near porous edges: Theory. In APS Division of Fluid Dynamics Meeting Abstracts, pages E03–013, 2020.

- [10] H. Chen and J. W. Jaworski. Noise generation by a vortex ring near porous and elastic edges. 2020. In AIAA Aviation 2020 Forum. Virtual Event: Paper AIAA-2020-2526.
- [11] H. Chen, Z. W. Yoas, J. W. Jaworski, and M. H. Krane. Acoustic emission of a vortex ring near a porous edge. Part 1: theory. *Journal of Fluid Mechanics*, 941:A28, 2022.
- [12] M. J. Colbrook and L. J. Ayton. A spectral collocation method for acoustic scattering by multiple elastic plates. *Journal of Sound and Vibration*, 461:114904, 2019.
- [13] M. J. Colbrook and A. Kisil. A Mathieu function boundary spectral method for scattering by multiple variable poro-elastic plates, with applications to metamaterials and acoustics. Proceedings of the Royal Society of London A, 476(2241):20200184, 2020.
- [14] M. J. Colbrook and M. J. Priddin. Fast and spectrally accurate numerical methods for perforated screens (with applications to Robin boundary conditions). IMA J. Appl. Math., 85(5):790–821, 2020.
- [15] D. G. Crighton. Acoustic edge scattering of elastic surface waves. Journal of Sound and Vibration, 22(1):25–32, 1972.
- [16] D. G. Crighton. Radiation from vortex filament motion near a half plane. Journal of Fluid Mechanics, 51(2):357–362, 1972.
- [17] D. G. Crighton. Airframe noise. In H. H. Hubbard, editor, Aerodynamic Theory: A General Review of Progress. Volume 1: Noise Sources. NASA Langley Research Center, 1991.
- [18] D. G. Crighton and D. Innes. The modes, resonances and forced response of elastic structures under heavy fluid loading. *Philosophical Transactions of the Royal Society* of London A, 312(1521):295–341, 1984.
- [19] D. G. Crighton and F. G. Leppington. Scattering of aerodynamic noise by a semi-infinite compliant plate. *Journal of Fluid Mechanics*, 43(4):721–736, 1970.

- [20] D. G. Crighton and F. G. Leppington. On the scattering of aerodynamic noise. *Journal of Fluid Mechanics*, 46(3):577–597, 1971.
- [21] N. Curle. The influence of solid boundaries upon aerodynamic sound. *Proceedings of the Royal Society of London A*, 231(1187):505–514, 1955.
- [22] W. Devenport, N. Alexander, S. Glegg, and M. Wang. The sound of flow over rigid walls. Annual Review of Fluid Mechanics, 50:435–458, 2018.
- [23] A. P. Dowling, M. M. Sevik, and J. Ffowcs Williams. Sound and sources of sound. The American Society of Mechanical Engineers (ASME), 1984.
- [24] J. E. Ffowcs Williams. The acoustics of turbulence near sound-absorbent liners. *Journal of Fluid Mechanics*, 51(4):737–749, 1972.
- [25] J. E. Ffowcs Williams and L. E. Hall. Aerodynamic sound generation by turbulent flow in the vicinity of a scattering half plane. *Journal of Fluid Mechanics*, 40(4):657–670, 1970.
- [26] M. R. Fink and D. A. Bailey. Airframe noise reduction studies and clean-airframe noise investigation. *United Technologies Research Center*, (NASA Contractor Report 159311), 1980.
- [27] T. Geyer, E. Sarradj, and C. Fritzsche. Measurement of the noise generation at the trailing edge of porous airfoils. *Experiments in Fluids*, 48(2):291–308, 2010.
- [28] M. Howe, M. Scott, and S. Sipcic. The influence of tangential mean flow on the rayleigh conductivity of an aperture. Proceedings of the Royal Society of London. Series A: Mathematical, Physical and Engineering Sciences, 452(1953):2303–2317, 1996.
- [29] M. S. Howe. Contributions to the theory of aerodynamic sound, with application to excess jet noise and the theory of the flute. *Journal of Fluid Mechanics*, 71(4):625–673, 1975.

- [30] M. S. Howe. On the added mass of a perforated shell, with application to the generation of aerodynamic sound by a perforated trailing edge. *Proceedings of the Royal Society* of London A, 365(1721):209–233, 1979.
- [31] M. S. Howe. On the generation of sound by turbulent boundary layer flow over a rough wall. *Proceedings of the Royal Society of London A*, 395(1809):247–263, 1984.
- [32] M. S. Howe. Sound produced by an aerodynamic source adjacent to a partly coated, finite elastic plate. Proceedings of the Royal Society of London A, 436(1897):351–372, 1992.
- [33] M. S. Howe. The compact Green's function for a semi-infinite elastic plate, with application to trailing edge noise and blade-vortex interaction noise. *The Journal of Acoustical Society of America*, 94(4):2353–2364, 1993.
- [34] M. S. Howe. Structural and acoustic noise produced by turbulent flow over an elastic trailing edge. *Proceedings of the Royal Society of London A*, 442(1916):533–554, 1993.
- [35] M. S. Howe. Structural and acoustic noise generated by turbulent flow over the edge of a coated section of an elastic plate. *Journal of Sound and Vibration*, 176(1):1–18, 1994.
- [36] M. S. Howe. Acoustics of fluid-structure interactions. Cambridge University Press, 1998.
- [37] M. S. Howe. Theory of vortex sound. Cambridge University Press, 2003.
- [38] M. S. Howe. Acoustics and aerodynamic sound. Cambridge University Press, United Kingdom, 2014.
- [39] J. W. Jaworski and N. Peake. Aerodynamic noise from a poroelastic edge with implications for the silent flight of owls. *Journal of Fluid Mechanics*, 723:456–479, 2013.
- [40] J. W. Jaworski and N. Peake. Aeroacoustics of silent owl flight. Annual Review of Fluid Mechanics, 52:395–420, 2020.

- [41] T. Kambe, T. Minota, and Y. Ikushima. Acoustic wave emitted by a vortex ring passing near the edge of a half-plane. *Journal of Fluid Mechanics*, 155:77–103, 1985.
- [42] M. R. Khorrami and M. M. Choudhari. Application of passive porous treatment to slat trailing edge noise. NASA Technical Report, 2003. TM-2003-212416.
- [43] A. Kisil and L. J. Ayton. Aerodynamic noise from rigid trailing edges with finite porous extensions. *Journal of Fluid Mechanics*, 836:117–144, 2018.
- [44] H. Lamb. Hydrodynamics. Cambridge University Press, 1924.
- [45] F. G. Leppington. Scattering of sound waves by finite membranes and plates near resonance. Quarterly Journal of Mechanics and Applied Mathematics, 29(4):527–546, 1976.
- [46] M. J. Lighthill. On sound generated aerodynamically. I. General theory. Proceedings of the Royal Society of London A, 211(1107):564–587, 1952.
- [47] M. J. Lighthill. Waves in fluids. Cambridge University Press, 2001.
- [48] N. W. McLachlan. Theory and application of Mathieu functions. 1951.
- [49] W. Möhring. On vortex sound at low Mach number. *Journal of Fluid Mechanics*, 85(4):685–691, 1978.
- [50] S. Moreau and M. Roger. Back-scattering correction and further extensions of Amiet's trailing-edge noise model. Part II: Application. *Journal of sound and vibration*, 323(1-2):397–425, 2009.
- [51] P. M. Morse and K. U. Ingard. Theoretical acoustics. Princeton University Press, 1986.
- [52] P. A. Nelson. Noise generated by flow over perforated surfaces. Journal of Sound and Vibration, 83(1):11–26, 1982.
- [53] F. W. Olver, D. W. Lozier, R. F. Boisvert, and C. W. Clark. NIST Handbook of Mathematical Functions. Cambridge University Press, 2010.

- [54] C. Pimenta, W. R. Wolf, and A. V. G. Cavalieri. A fast numerical framework to compute acoustic scattering by poroelastic plates of arbitrary geometry. *Journal of Computational Physics*, 373:763–783, 2018.
- [55] I. Podlubny. Fractional differential equations. Elsevier, 1998.
- [56] A. Powell. Theory of vortex sound. The Journal of Acoustical Society of America, 36(1):177–195, 1964.
- [57] L. Rayleigh. The theory of sound, volume 2. Dover, 1945.
- [58] M. Swann, Z. Yoas, P. Trzcinski, H. Chen, M. Krane, and J. Jaworski. Aeroacoustics of porous trailing edges. In APS Division of Fluid Dynamics Meeting Abstracts, 2021.
- [59] L. N. Trefethen. Spectral methods in MATLAB. SIAM, 2000.
- [60] Z. W. Yoas. Passive trailing edge noise attenuation with porosity, inspired by owl plumage. Master's thesis, Pennsylvania State University, August 2021.

Biography

Huansheng Chen graduated with a Bachelor of Engineering degree in Aeronautical and Astronautical Engineering at Beihang University (previously known as Beijing University of Aeronautics and Astronautics) in China. In August 2016, he came to Lehigh to pursue graduate study and started to do research in fluid-structure interactions with Dr. Justin W. Jaworski in Feburary 2017, and completed a Master's degree in May 2018. As a graduate student, Huansheng has published two journal papers (JFS & JFM) and six conference preceedings and been supported by external grants from the Air Force Office of Scientific Research (AFOSR) and National Science Foundation (NSF) to support his research activities. He was awarded various fellowship at Lehigh such as the J. David A. Walker and M. Elizabeth Walker Endowed Fellowship, Rossin College Doctoral Fellowship Award and the department of Mechanical Engineering and Mechanics Fellowship. He was also awarded the Doctoral Travel Grant for Global Opportunities (DTG-GO) in 2019 to support his international trip to the 23rd International Congress on Acoustics. Huansheng is a member of AIAA and APS.